





A pH-responsive PROTAC-based nanosystem triggers tumor-specific ferroptosis to construct in situ tumor vaccines

Linghong Huang^{a,b,1} , Xinyuan Sun^{b,1} , Qinhua Zuo^{a,1}, Ting Song^a, Ning Liu^{c,*}, Zonghua Liu^{a,**}, Wei Xue^{a,***}

^a Department of Biomedical Engineering, Jinan University, Guangzhou, 510632, China

^b Department of Urology, Guangdong Provincial Key Laboratory of Urological Diseases, The First Affiliated Hospital of Guangzhou Medical University, Guangzhou Medical University, Guangzhou, 510230, China

^c Department of Bone and Joint Surgery, The First Affiliated Hospital of Jinan University, Jinan University, Guangzhou, 5106323, China

ARTICLE INFO

Keywords:

In situ tumor vaccines
Antigen presentation
PROTAC
Ferroptosis

ABSTRACT

Bromodomain-containing protein 4 (BRD4) is a key protein that drives the development of malignant melanoma and is closely associated with the ferroptosis signaling pathway. Degradation of BRD4 can downregulate the expression of ferroptosis-related genes such as GPX4, thereby promoting tumor-specific ferroptosis. Therefore, targeting BRD4 for degradation is a promising strategy for inhibiting tumor growth. We constructed a PROTAC drug-based tumor antigen capture system to protect the activity of antigen-presenting cells (APCs) and promote antigen capture. The selected PROTAC drug (ARV-825) can specifically degrade BRD4 without harming immune cells. Specifically, magnetic nanoclusters (MNC) coated with calcium-doped manganese carbonate (Ca/MnCO₃), were used to load PROTAC drug (ARV-825) and anti-PD1, forming the MNC@Ca/MnCO₃/ARV/anti-PD1 system. ARV-825 can specifically degrade BRD4 and GPX4, significantly inducing ferroptosis in tumor cells and releasing tumor-associated antigens. The MNC@Ca/MnCO₃ particles, with their large specific surface area, adsorbed the tumor antigens, preventing antigen loss and enhancing antigen presentation. Additionally, Mn²⁺ served as an adjuvant to promote the maturation and cross-presentation of APCs. Together with the PD1 antibody, this further enhanced the anti-tumor response of the in situ tumor vaccine and reversed the suppressive immune microenvironment. This antigen capture system provides a novel strategy to improve the anti-tumor efficacy of in situ tumor vaccines.

1. Introduction

Malignant melanoma, characterized by its high invasiveness and metastatic potential, remains a major challenge in the field of oncology. Bromodomain-containing protein 4 (BRD4) has been identified as a crucial protein in regulating the cell cycle and differentiation of melanoma cells [1]. BRD4 belongs to the bromodomain and extra terminal domain (BET) protein family and plays a central role in the epigenetic regulation of gene expression. By binding to acetylated lysine residues on histone tails, BRD4 functions as a transcriptional regulator, promoting the recruitment of transcriptional machinery and enhancing gene transcription. In melanoma, BRD4 is overexpressed and

hyperactive, contributing to uncontrolled cancer cell growth and survival [1]. Additionally, studies have revealed a significant connection between BRD4 and the ferroptosis signaling pathway [2]. Ferroptosis is characterized by iron-dependent accumulation of lipid peroxides and has emerged as a novel therapeutic approach for cancers, especially those resistant to traditional therapies. BRD4 regulates the expression of key genes involved in the ferroptosis process, such as GPX4, a crucial enzyme that protects cells from ferroptosis-induced lipid peroxide accumulation [3]. Therefore, the specific degradation of BRD4 is an effective strategy to downregulate GPX4 expression and induce tumor-specific ferroptosis, thereby inhibiting melanoma growth. However, inducing ferroptosis in melanoma cells alone is insufficient to

* Corresponding author.

** Corresponding author.

*** Corresponding author.

E-mail addresses: liuning@163.com (N. Liu), tliuzonghua@jnu.edu.cn (Z. Liu), weixue_jnu@aliyun.com (W. Xue).

¹ These authors contributed equally to this work and should be considered as co-first authors.

inhibit tumor metastasis. Thus, further blocking metastasis remains a critical challenge.

Constructing in situ tumor vaccines is a crucial strategy for further enhancing antitumor efficacy [4–6]. In the mechanism of in situ tumor vaccines, tumor cells are killed, releasing tumor antigens, which are captured by antigen-presenting cells (APCs) and presented to T lymphocytes, inducing specific cytotoxic T lymphocytes (CTLs) to directly kill tumor cells. However, the antitumor effect of in situ tumor vaccines is generally weak [7], primarily due to the low efficiency of antigen capture and presentation by APCs. Tumor antigens released after tumor cell death are often rapidly cleared and cannot be effectively captured by APCs. Therefore, improving antigen capture is key to initiating an antitumor immune response. To enhance antigen capture efficiency, researchers have proposed several strategies. For instance, maleimide molecules improve antigen capture by forming thioether bonds with released tumor antigens [8]; poly(amidoamine) dendrimers capture tumor antigens through ionic bonds [9]; and adhesive hydrogel three-dimensional network structures are used to capture tumor antigens in situ, achieving sustained release of tumor antigens [10]. Exploring more antigen capture strategies is essential for enhancing antigen presentation and thereby improving the efficacy of in situ tumor vaccines. Therefore, we further constructed an in situ tumor vaccine based on the induction of ferroptosis in melanoma cells to enhance the anti-tumor immune response for long-lasting resistance against tumors.

To target the degradation of BRD4 and enhance antitumor immune responses, we developed a tumor antigen capture system based on proteolysis-targeting chimeras (PROTAC) drugs. PROTAC is a bifunctional molecule designed to recruit target proteins to the cell's ubiquitin-proteasome system for degradation, thereby specifically inhibiting protein function [11–14]. PROTAC drugs offer significant advantages in anti-tumor therapy by specifically targeting proteins with high precision, minimizing off-target effects, and enhancing treatment safety and efficacy [15]. Their unique protein degradation mechanism also overcomes drug resistance issues common in traditional therapies, opening new therapeutic avenues [16]. As research advances, PROTACs are poised to become a cornerstone of personalized medicine, offering more efficient and tailored treatment options for cancer patients. Studies have shown that PROTAC drugs can also reverse the immunosuppressive tumor microenvironment and enhance antitumor immunity [17,18]. Therefore, we chose the BRD4-degrading PROTAC drug ARV-825 as part of our system. The system employs magnetic nanoclusters (MNCs) coated with calcium/manganese carbonate (Ca/MnCO_3) as carriers for the PROTAC drug and anti-PD1 antibody, forming the $\text{MNC@Ca/MnCO}_3/\text{ARV}/\text{anti-PD1}$ complex. This configuration allows for the targeted delivery of ARV-825 and PD1 blockers directly to the tumor microenvironment, optimizing therapeutic efficacy while minimizing off-target effects on immune cells. ARV-825 specifically degrades BRD4 and GPX4 in melanoma cells, inducing ferroptosis, promoting the release of tumor-associated antigens, and maintaining the activity of APCs. Ca/MnCO_3 particles are biocompatible and have a large specific surface area, enabling efficient adsorption of tumor antigens, preventing antigen loss, and enhancing the antigen-presenting capability of APCs. Additionally, in our previous study, we found that MNC magnetic nanoparticles alone had a very limited effect on the activation of dendritic cells (DCs). In contrast, the introduction of Ca^{2+} and Mn^{2+} , which have immunostimulatory effects, significantly enhanced the immunostimulatory effect and dramatically increased the activation level and antigen-presenting capacity of DCs [19]. Moreover, Ca/MnCO_3 are acid-sensitive and can be designed as pH-sensitive drug delivery systems. Tumor microenvironments are usually slightly acidic, so these compounds can be dissolved in response to acidic conditions upon arrival at the tumor site, thus facilitating effective drug release. This synergistic effect, combined with PD1 blockade, further enhances the antitumor response of in situ tumor vaccines, reversing the immunosuppressive microenvironment characteristic of melanoma. This integrated approach highlights the combination of targeted protein

degradation and immune modulation to overcome the challenges posed by malignant melanoma, providing new avenues for cancer therapeutic strategies.

2. Results and discussion

2.1. The synthesis and characterization of MNC@Ca/MnCO_3 nanoparticles

Multifunctional magnetic nanoparticles MNC@Ca/MnCO_3 with flower-like core/shell structure were synthesized by a one-pot method via forming Ca/MnCO_3 coating around the core of MNC (Fig. 1A). The flower-like core/shell structure usually exhibits excellent antigen loading capacity. The images of scanning electron microscope (SEM) and transmission electron microscope (TEM) depicted that the MNC were spherical with sizes of ~ 80 nm (Fig. 1B), and the MNC@Ca/MnCO_3 nanoparticles were flower-like with sizes of ~ 800 nm (Fig. 1C and D). The X-ray powder diffractometer (XRD) patterns of MNC@Ca/MnCO_3 nanoparticles as shown in Fig. 1E. The diffraction peaks in 24.19° , 31.31° , and 41.33° corresponded to the (012), (104), and (113) crystal planes of MnCO_3 (JCPDS no. 44–1472), respectively. While the diffraction peaks in 30.36° , 35.76° , and 43.47° corresponded to the (220), (311), and (400) crystal planes of MNC (JCPDS no. 65–3017) [20], respectively. Subsequently, the infrared spectrum (IR) showed that (Fig. 1F), the appearance of the peak around 585 cm^{-1} is due to the stretching vibration of Fe-O-Fe [21], while the appearance of peaks at 1452 cm^{-1} and 871 cm^{-1} is due to the stretching and bending vibrations of CO_3^{2-} [22], respectively. These results indicate that MNC@Ca/MnCO_3 nanoparticles were successfully synthesized. In addition, the hysteresis regression curves of the particles showed that the MNC covered by Ca/MnCO_3 still maintained good magnetic properties (Fig. 1G). The size of MNC@Ca/MnCO_3 particles was predominantly distributed at 712 nm and had a polydispersity index (PDI) of 0.68 (Supporting Information Figure S2C).

In addition, the MNC@Ca/MnCO_3 particles were characterized using XPS. The full XPS spectrum (Supporting Information Figure S1A) revealed binding energy peaks for Ca 2p, Mn 2p, Fe 2p, C 1s, and O 1s, confirming the presence of Ca, Mn, Fe, C, and O elements within the particles. Specifically, peaks at 347.1 eV and 350.7 eV are attributed to Ca 2p_{3/2} and Ca 2p_{1/2}, while those at 641.9 eV and 653.8 eV correspond to Mn 2p_{3/2} and Mn 2p_{1/2}, respectively (Figs. S1B and C), indicating the presence of Ca^{2+} and Mn^{2+} in the particles. Peaks at 710.4 eV and 724.1 eV, corresponding to Fe 2p_{3/2} and Fe 2p_{1/2} (Fig. S1D), show that the surface modification with Ca/MnCO_3 did not alter the valence states of the MNC, preserving their magnetic properties. Additionally, characteristic C 1s and O 1s peaks were observed in the spectra (Figs. S1E and F), further supporting the successful synthesis of MNC@Ca/MnCO_3 particles. According to our measurements (Supporting Information Figures S1G&H), the MNC@Ca/MnCO_3 nanoparticles exhibited a large specific surface area ($53.8\text{ m}^2/\text{g}$) and a large average pore size (5.5 nm), which meets the definition of mesoporous materials. This remarkable specific surface area provides abundant adsorption sites for drugs, while the mesoporous structure facilitates effective drug accommodation.

2.2. ARV-825 and PD-1 antibody loading and releasing capacity of MNC@Ca/MnCO_3 nanoparticles

Firstly, the absorption spectra of different concentrations of ARV-825 were detected in the wavelength range of 300–600 nm, and the results showed that ARV-825 had maximum absorption at 412 nm (Fig. 2A). Then, the ARV-825 loading ratio of MNC@Ca/MnCO_3 nanoparticles was examined, as shown in Fig. 2B. 5 mg of MNC@Ca/MnCO_3 nanoparticles completely adsorbed 1 mg of ARV-825 within 0.5 h and maintained a stable loading of ARV-825 for a long time. This proves that MNC@Ca/MnCO_3 nanoparticles quickly loaded a large number of ARV-825.

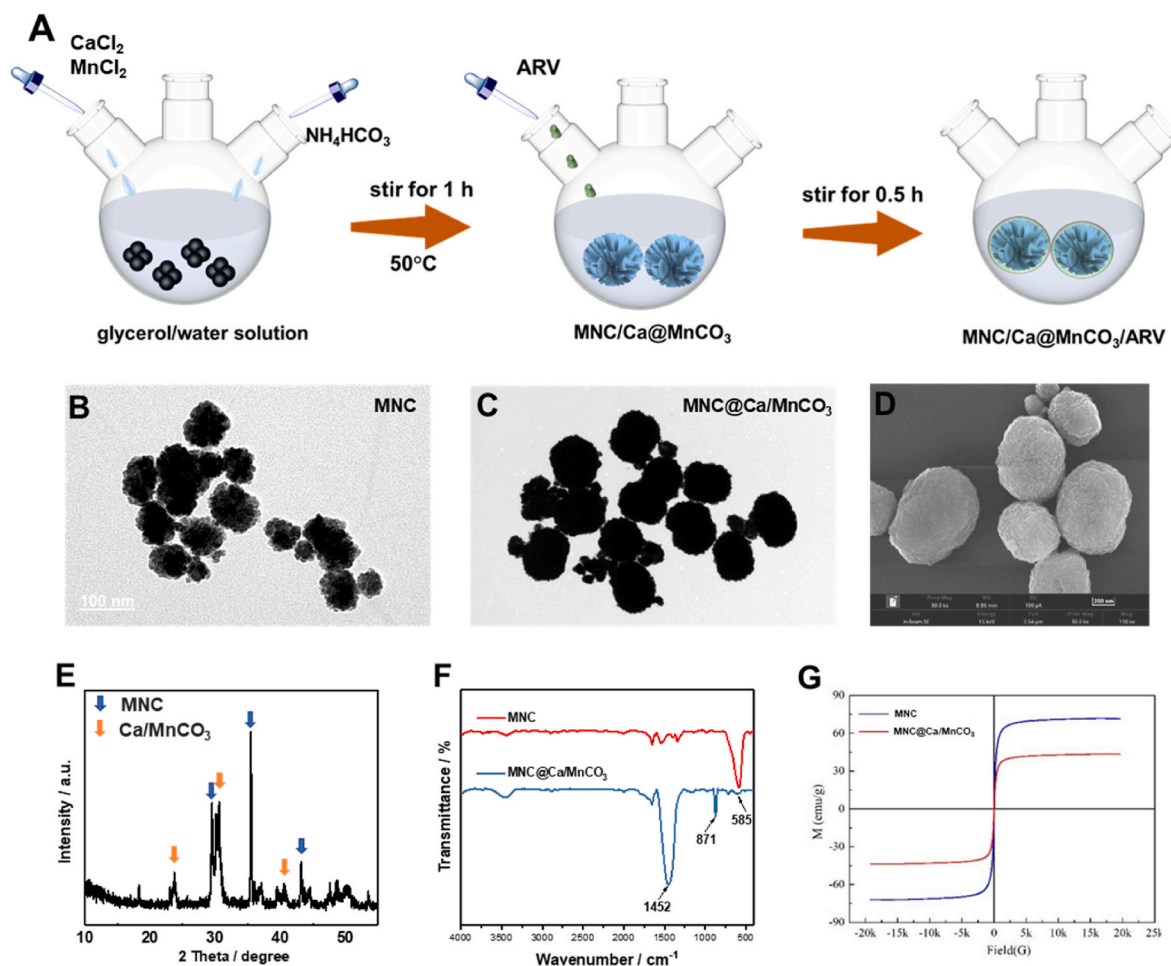


Fig. 1. (A) The synthetic schematic diagram of MNC@Ca/MnCO₃ nanoparticles. The TEM images of (B) MNC and (C) MNC@Ca/MnCO₃ nanoparticles. (D) The SEM image of MNC@Ca/MnCO₃ nanoparticle. (E) The XRD spectrum of MNC@Ca/MnCO₃ nanoparticles. (F) The FT-IR spectra of MNC and MNC@Ca/MnCO₃ nanoparticles. (G) The hysteresis regression curves of MNC and MNC@Ca/MnCO₃ nanoparticles.

Meanwhile, The IR spectra showed (Fig. 2C) that the MNC@Ca/MnCO₃ nanoparticles loaded with ARV-825 contained characteristic peaks of ARV-825 at 1641, 1451, 1086, 869, and 577 cm⁻¹. Meanwhile, the MNC@Ca/MnCO₃ nanoparticles loaded with ARV-825 were found to be green and magnetic (Fig. 2D). In addition, the surface charges of MNC, MNC@Ca/MnCO₃, and MNC@Ca/MnCO₃/ARV nanoparticles were -4.46 mV, -13.1 mV and -19.3 mV, respectively. This indicates a significant change in the surface charge of the particles after loading ARV-825. All these results indicate that ARV-825 was successfully loaded by MNC@Ca/MnCO₃ nanoparticles, and the elemental contents in the MCM/ARV nanoparticles determined using ICP were Fe (14.1 %, w/w), Ca (14.8 %, w/w), and Mn (11.3 %, w/w), respectively. Subsequently, the anti-PD1 loading ratio of MNC@Ca/MnCO₃/ARV nanoparticles was examined with BCA kits. As shown in Supporting Information Figure S1A, 1 mg of MNC@Ca/MnCO₃/ARV nanoparticles completely adsorbed 24 μg of anti-PD1 within 1 h and maintained a stable loading of anti-PD1 for a long time. This proves that anti-PD1 could be stably loaded by MNC@Ca/MnCO₃/ARV nanoparticles. In addition, to explore the pH-sensitive capability of the MNC@Ca/MnCO₃ nanoparticles and the release ratio of ARV-825, MNC@Ca/MnCO₃/ARV nanoparticles were placed into different pH buffers, the results were shown in Fig. 2E. The MNC@Ca/MnCO₃ nanoparticles released ARV-825 slowly in the weak acid buffer, indicating that nanoparticles are pH sensitive. We further evaluated the release of PD-1 antibody under both conditions using a BCA assay kit. The results, as shown in Supporting Information Figure S3D, indicate that PD-1 antibody also

undergoes slow release in the acidic buffer while remaining stable in the neutral buffer, with no significant release observed. These findings confirm that the carrier degrades gradually in an acidic solution, leading to the subsequent release of both ARV-825 and PD-1 antibody adsorbed onto it. This behavior underscores the pH-responsive nature of the MNC@Ca/MnCO₃ nanoparticles and their potential for drug release in lysosomes.

Subsequently, we characterized the morphology and particle size of MNC@Ca/MnCO₃/ARV and MNC@Ca/MnCO₃/ARV/anti-PD1 particles. As shown in Supporting Information Figures S3A&B, both composite particles maintained a flower-like structure, and this specific morphology helped to enhance their drug loading capacity. The particle size of MNC@Ca/MnCO₃/ARV and MNC@Ca/MnCO₃/ARV/anti-PD1 particles were as shown in Supporting Information Figures S3C, the MNC@Ca/MnCO₃/ARV, and MNC@Ca/MnCO₃/ARV/anti-PD1 particles showed a slight increase in the particle size compared to the original MNC@Ca/MnCO₃ particles, which was attributed to the fact that MNC@Ca/MnCO₃/ARV particles showed adsorption of a large amount of ARV-825. whereas, compared to MNC@Ca/MnCO₃/ARV particles, the MNC@Ca/MnCO₃/ARV/anti-PD1 particles did not significantly increase in particle size. Finally, we used transmission electron microscopy (TEM) combined with energy dispersive X-ray spectroscopy (EDS) to analyze the spatial distribution of the elements within the nanoparticles. The results were shown in the Supporting Information Figure S2E, where the Fe element was observed in the core of the nanoparticles, which was attributed to the MNCs, verifying that the

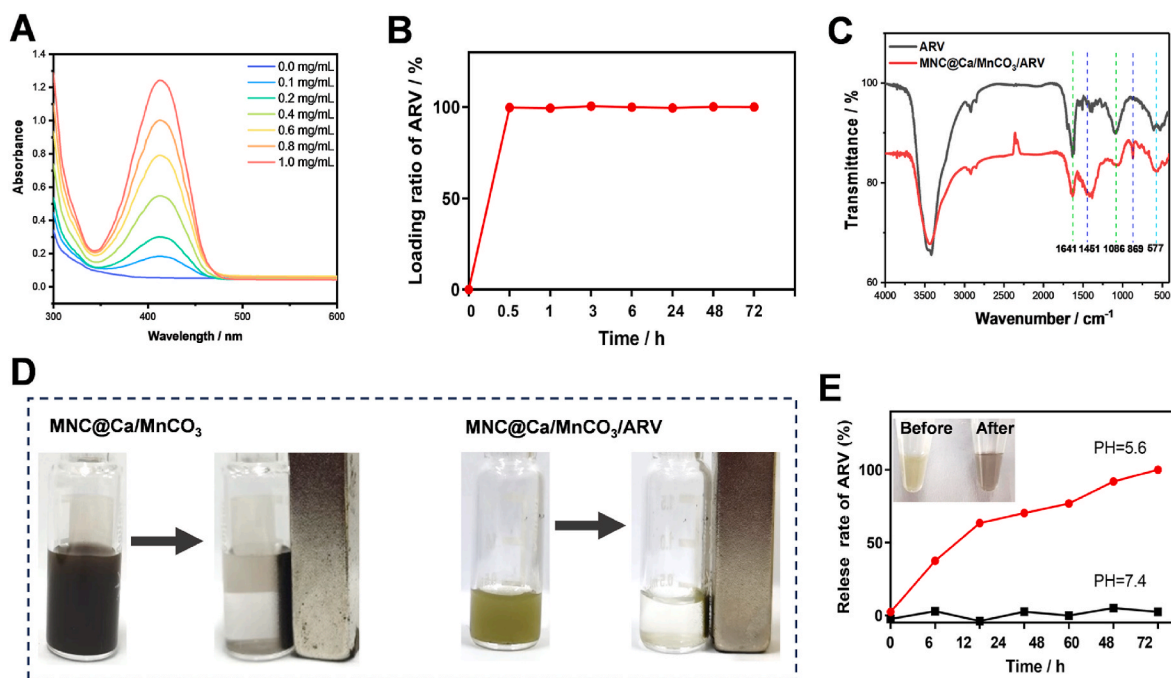


Fig. 2. (A) The absorption curves of different concentrations of ARV-825. (B) The ARV-825 loading rates of MNC@Ca/MnCO₃ nanoparticles at different times. (C) The FT-IR spectra of ARV and MNC@Ca/MnCO₃/ARV nanoparticles. (D) The magnetic properties of ARV and MNC@Ca/MnCO₃/ARV nanoparticles. (E) The ARV releasing rates of MNC@Ca/MnCO₃/ARV nanoparticles in the neutral and weak acid buffer.

MNCs acted as the basis of the internal structure of the system. The Ca, Mn, C, and O elements, which were attributed to the Ca/MnCO₃, confirmed that calcium-doped manganese carbonate was successfully encapsulated in the outer layer of the MNC, forming the intermediate layer of the system. Whereas the N element and a small amount of S element were observed in the outermost layer of the nanoparticles, with the N element attributed to the ARV-825, while the S element originated from the PD1 antibody, suggesting that the ARV-825 and the PD1 antibody successfully modified the on the surface of the nanoparticles, constituting the outermost layer of the system. Through the above EDS mapping analysis, we confirmed that the components of the nanoparticles were accurately assembled as expected, and their spatial distribution was highly consistent with the schematic diagram.

2.3. The cytotoxicity of MNC@Ca/MnCO₃ nanoparticles on tumors and DCs

To reveal the in vitro toxicity of the ARV-825, MNC@Ca/MnCO₃ or MNC@Ca/MnCO₃/ARV, DCs or B16 cells were incubated with different concentrations of ARV-825, MNC@Ca/MnCO₃ and MNC@Ca/MnCO₃/ARV. As shown in Fig. 3A, the cellular toxicity of ARV and MNC@Ca/MnCO₃/ARV nanoparticles on B16 cells overall dropped with the increased concentrations, and the toxicity of MNC@Ca/MnCO₃/ARV nanoparticles on B16 cells was greater than ARV-825. When the concentration of ARV-825 was 200 ng/mL, the cell viability of the ARV alone group significantly decreased to 79.7 %, while the cell viability of the MNC@Ca/MnCO₃/ARV group significantly decreased to 32.1 %, manifesting a more brilliant tumor therapeutic effect. In addition, co-cubation of different concentrations of ARV-825 or MNC@Ca/MnCO₃ nanoparticles with DCs for 24 h did not affect the cell viability of DCs, indicating that ARV-825 or MNC@Ca/MnCO₃ nanoparticles have very low cytotoxicity for DCs (Fig. 3B and C). Thus, the ARV-825 at a concentration of 200 ng/mL was selected for subsequent experiments. In addition, the toxicity of different concentrations of MNC@Ca/MnCO₃/ARV nanoparticles on DC2.4 was measured. As shown in Supporting Information Figure S3C, the MNC@Ca/MnCO₃/ARV nanoparticles were not toxic to DC2.4 when the concentration of ARV was below 1000 ng/

mL. In this study, the concentration of ARV in the MNC@Ca/MnCO₃/ARV nanoparticles acting on B16 cells was 200 ng/mL, which was much lower than 1000 ng/mL, and thus non-toxic to normal immune cells at this concentration. Thus, the MNC@Ca/MnCO₃ nanoparticles were biosafety carriers. Subsequently, the cell morphologies were observed after treatment with each group, and the results were shown in Supporting Information Figure S2A. The B16 cells treated with the ARV-825-containing group became disordered in cell morphology, decreased in cell number, and had a significant increase in cell mortality. Additionally, direct differentiation between living (green) and dead (red) cells was achieved through calcein-AM/PI fluorescence co-staining, as illustrated in Fig. 3D. The images exhibited that red fluorescent in the MNC@Ca/MnCO₃/ARV group were higher than that in other groups. The flow quantification results similarly showed that MNC@Ca/MnCO₃/ARV group induced significantly higher cell mortality than the other groups (Fig. 3E and F), indicating that the loading of MNC@Ca/MnCO₃ on ARV significantly increased the tumor cell killing efficiency. Furthermore, the loading of ARV-825 by MNC@Ca/MnCO₃ nanoparticles significantly inhibits cell migration (Fig. 3G and H). These results indicate that the MNC@Ca/MnCO₃ group did not affect cell migration compared with the blank control group, and the loading of ARV-825 by MNC@Ca/MnCO₃ nanoparticles significantly increased the toxicity, and inhibited cell migration of B16 cells.

2.4. MNC@Ca/MnCO₃ nanoparticles carry ARV-825 into lysosomes

The entry of ARV-825 into tumor cells is the most critical prerequisite for killing tumor cells. To demonstrate whether the loading of ARV-825 by MNC@Ca/MnCO₃ nanoparticles for increased cellular uptake of ARV-825, ARV-825, and MNC@Ca/MnCO₃/ARV nanoparticles were treated with B16 cells for 6 h. The results are shown in Fig. 4, ARV-825 was detected as an intense green fluorescence at 488 nm excitation wavelength (Fig. 4A–C). Quantitative flow cytometric analysis revealed that the intracellular fluorescence signal of the MNC@Ca/MnCO₃/ARV group was approximately 20-fold higher compared to the ARV-825 group (Fig. 4D and E). In addition, confocal laser scanning microscope (CLSM) images further showed that the intracellular ARV-825 in the

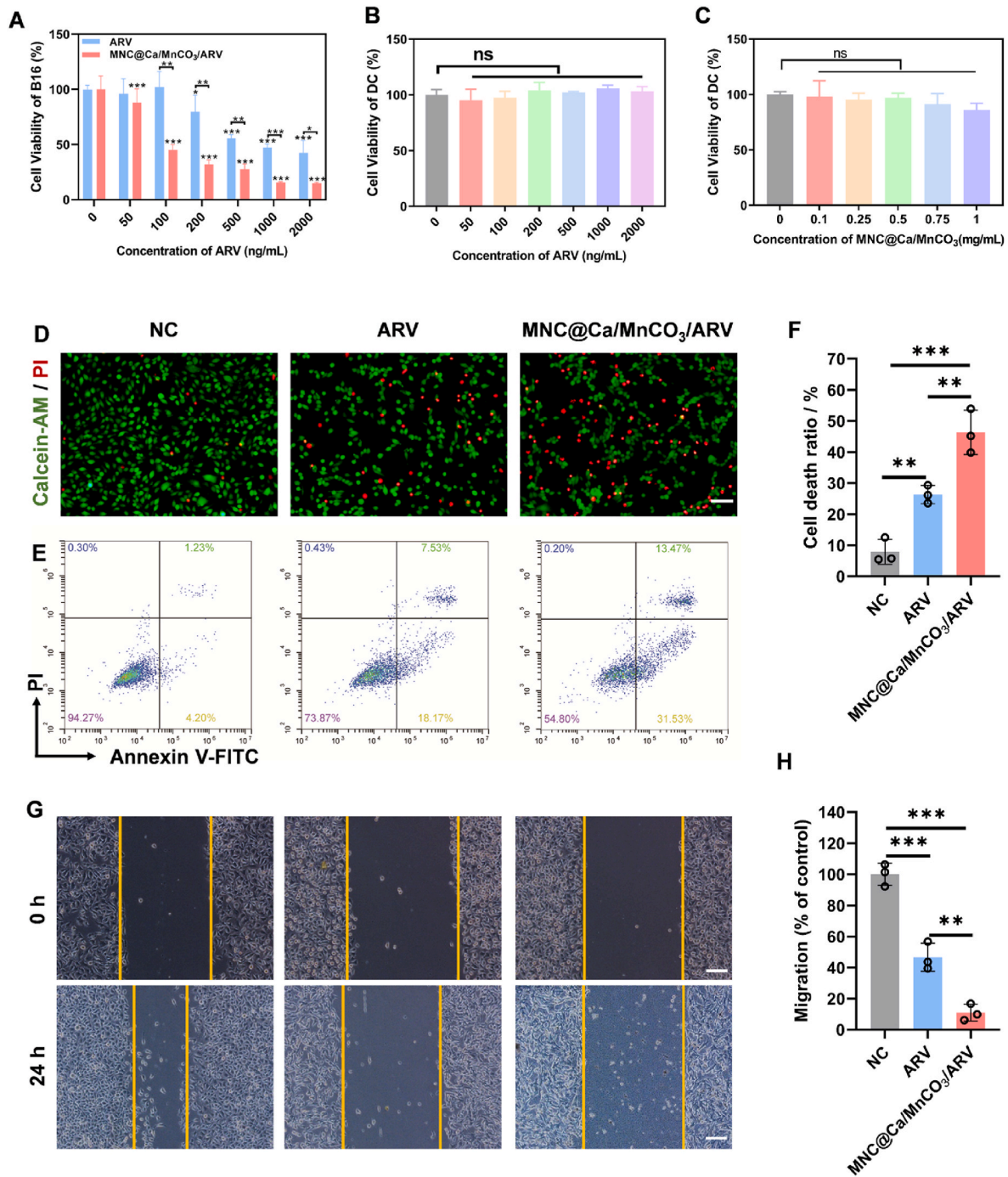


Fig. 3. (A) The cytotoxicity of B16 cells were incubated with different concentrations of ARV and MNC@Ca/MnCO₃/ARV. (B, C) The cytotoxicity of DC were incubated with different concentrations of ARV and MNC@Ca/MnCO₃. (D) The live and dead cell staining of B16 cells exposed to ARV and MNC@Ca/MnCO₃/ARV. (E–F) The apoptosis and necrosis assay of ARV and MNC@Ca/MnCO₃/ARV-treated B16 cells by flow cytometer. (G–H) The cell migration of B16 cells exposed to ARV, MNC@Ca/MnCO₃, and MNC@Ca/MnCO₃/ARV particles and the corresponding quantitative data. Scar bar: 100 μ m * P < 0.05, ** P < 0.01, *** P < 0.001.

MNC@Ca/MnCO₃/ARV group was significantly higher than the ARV group (Fig. 4F–H), validating that the loading of ARV-825 by MNC@Ca/MnCO₃ nanoparticles promoted internalization of the ARV-825 into tumor cells. This may be because the water solubility of ARV-825 is very low and the loading of ARV-825 by nanoparticles can significantly improve its dispersion in water.

2.5. Ferroptosis of B16 cells induced by in vitro degradation of BRD4 and GPX4

Ferroptosis is characterized by decreased mitochondrial membrane potential (MMP) and enhanced mitochondrial fragment [23,24], which can be detected by JC-1 dye. When mitochondrial membrane potential ($\Delta\psi$ m) is high, JC-1 aggregates within healthy mitochondria to form J-aggregates that emit red fluorescence; under these conditions, we use the red fluorescence channel for detection (with an excitation maximum at 585 nm and an emission maximum at 590 nm). Conversely, when

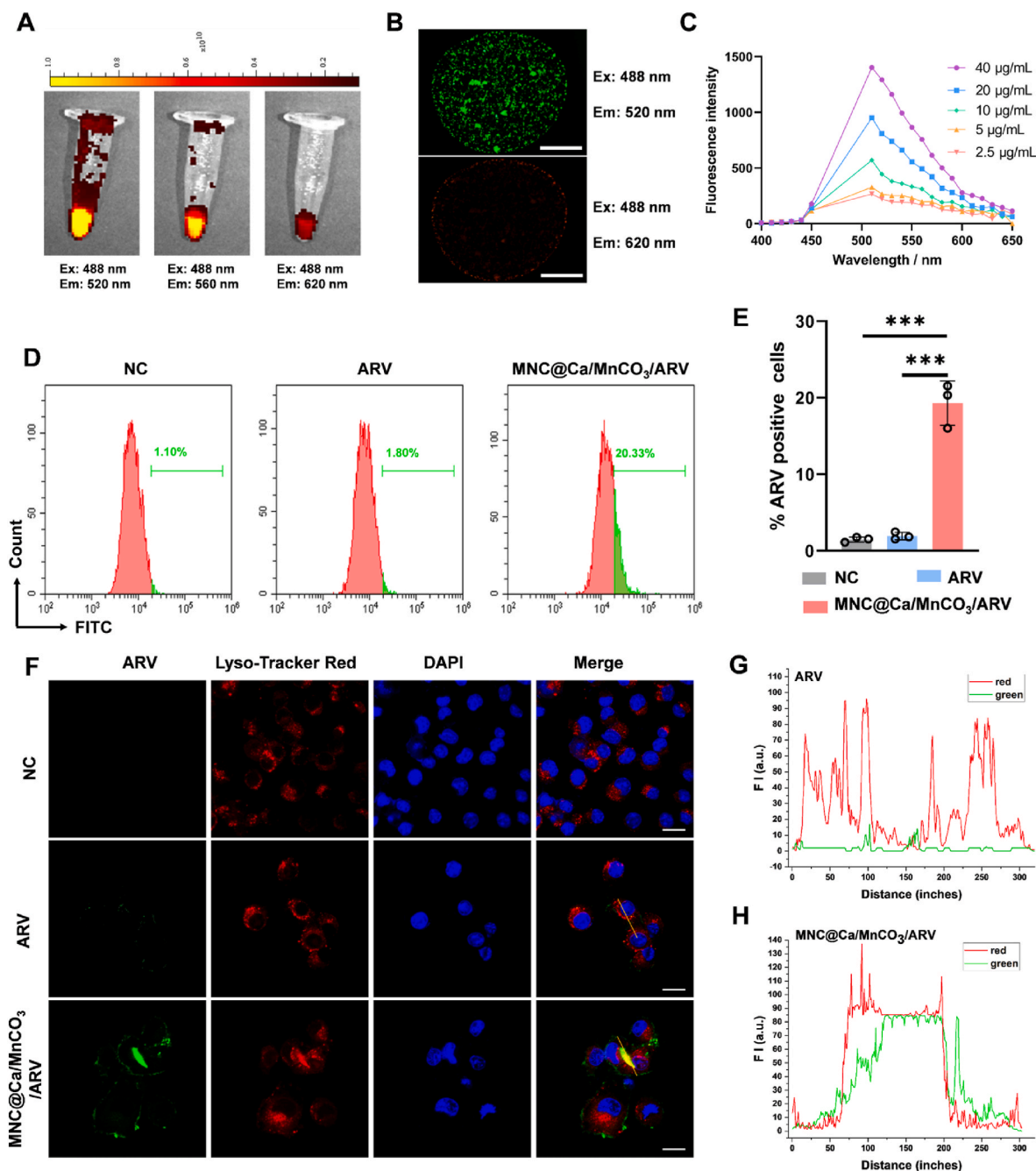


Fig. 4. (A) The fluorescence images of ARV at different emission wavelengths (excitation wavelength: 488 nm). (B) The fluorescence images of MNC@Ca/MnCO₃/ARV at different emission wavelengths (excitation wavelength: 488 nm), scar bar: 50 µm. (C) The fluorescence curves of different concentrations of ARV. (D–E) The internalized ARV by B16 cells and the corresponding statistical analysis in each group. (F) CLSM images of B16 cells after incubation with ARV or MNC@Ca/MnCO₃/ARV for 6 h, (G–H) and the corresponding co-localization of lysosomes and ARV. Scar bar: 20 µm, ***P < 0.001.

$\Delta\psi_m$ decreases or becomes depolarized, JC-1 exists as monomers within mitochondria, emitting green fluorescence; for this state, we opt for the green fluorescence channel for measurement (with an excitation maximum at 488 nm and an emission maximum at 525 nm). By comparing the enhancement of green fluorescence relative to red fluorescence, we can assess the decline in mitochondrial $\Delta\psi_m$. The results of the JC1 assay (Fig. 5A and B) revealed a progressive enhancement in the green fluorescence intensity of monomers in both the ARV and MNC@Ca/MnCO₃/ARV groups compared to the blank control group. Notably, the green fluorescence was significantly higher in the MNC@Ca/MnCO₃/ARV group than in the ARV group. Flow cytometry analysis further corroborated these findings, demonstrating a

significantly elevated green fluorescence intensity in the MNC@Ca/MnCO₃/ARV group compared to both the control and ARV-825 alone groups, as evidenced by the increased JC-1 monomer/aggregate ratio (Supporting Information Figures S2B&C). These results indicated that MNC@Ca/MnCO₃/ARV particles can significantly decline the MMP and $\Delta\psi_m$ of tumor cells. This finding not only underscores the impact of MNC@Ca/MnCO₃/ARV particles on mitochondrial function but also demonstrates their potential as inducers of ferroptosis.

In addition, ferroptosis manifested as increased lipid peroxidation and elevated ROS. Thus, the total intracellular production of ROS, O₂⁻, and lipid peroxide (LPO) of B16 cells was then assessed by DCFH-DA, DHE, and Liperflu fluorescent dyes, respectively. As shown in

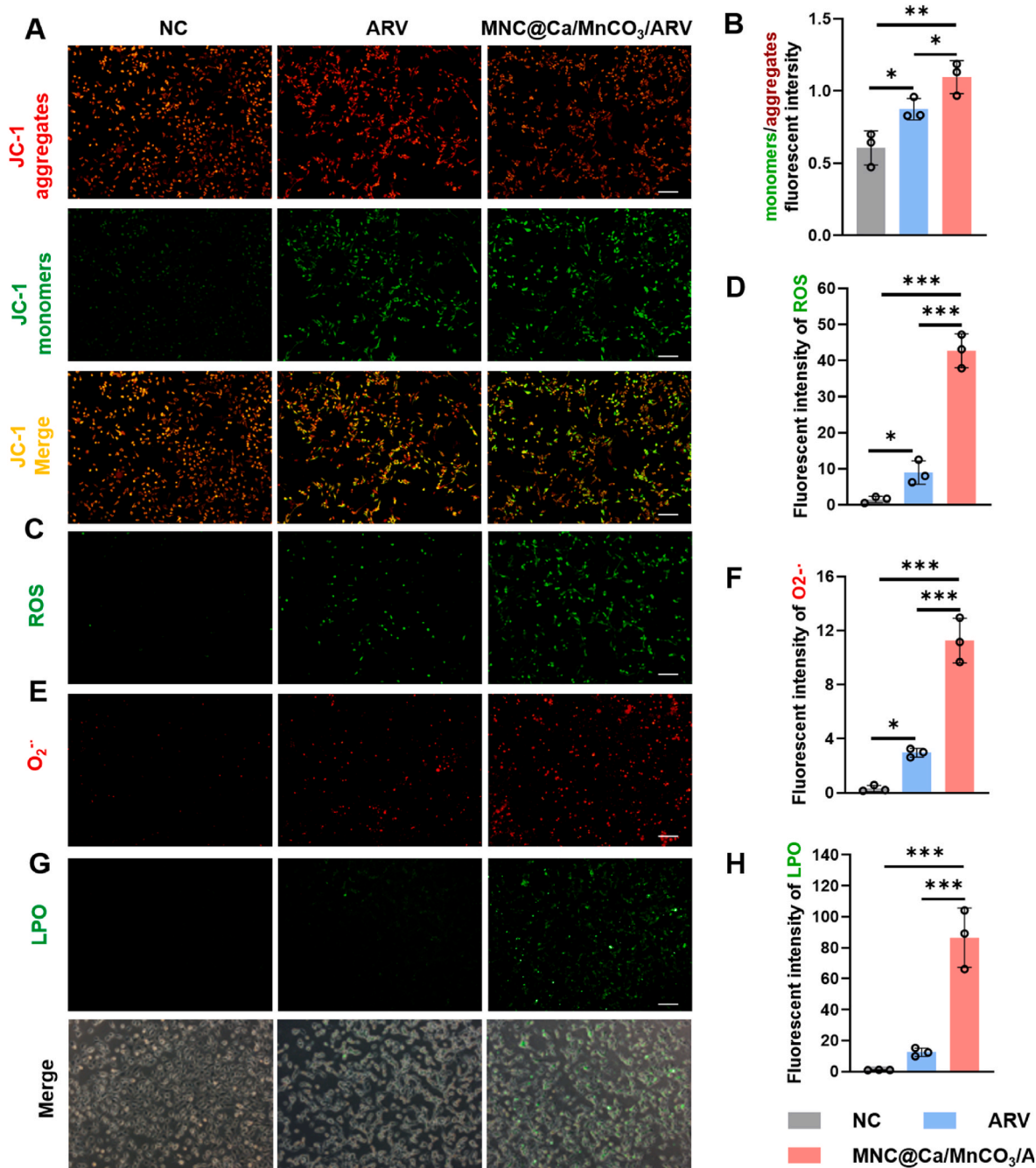


Fig. 5. (A–B) JC-1 fluorescence staining images of B16 cells and corresponding statistical analysis. (C–D) The intracellular ROS level of B16 cells and corresponding statistical analysis. (E–F) The intracellular O₂⁻ level of B16 cells and corresponding statistical analysis. (G–H) The LPO level of B16 cells and corresponding statistical analysis. Scar bar: 100 μm *P < 0.05, **P < 0.01, ***P < 0.001.

Fig. 5C–F, ARV and MNC@Ca/MnCO₃/ARV groups significantly promoted the production of ROS and O₂⁻, and the loading of ARVs by MNC@Ca/MnCO₃ nanoparticles further increased the production of ROS and O₂⁻. Consistent with the MMP assay, the results of LPO staining of tumor cells revealed that the production of LPO in the MNC@Ca/MnCO₃/ARV group significantly increased than that in control and ARV alone groups (Fig. 5G–H), which all indicated that the loading of ARV-825 by MNC@Ca/MnCO₃ nanoparticles can significantly promote the ferroptosis of B16 cells. Meanwhile, ROS can promote anti-tumor signaling and initiate oxidative stress-induced tumor cell death [25]. TEM was then used to directly observe the mitochondrial damage in paradigms of ferroptosis. As depicted in Fig. 6A, the mitochondrial morphologies observed in both the ARV and MNC@Ca/MnCO₃/ARV

groups exhibited more reduced mitochondrial size and pronounced mitochondrial fragmentation (indicated by red arrows) compared to the control group. Moreover, the mitochondrial cristae reduced and became disrupted in MNC@Ca/MnCO₃/ARV group. These results all indicated that the loading of ARV-825 by MNC@Ca/MnCO₃ nanoparticles aggravates ferroptosis of B16 cells.

In addition, we treated B16 and DC2.4 cells with MNC@Ca/MnCO₃/ARV particles, and subsequently evaluated the effect of these particles on both cell types by detecting the LPO accumulation levels. According to the results shown in Supporting Information Figures S4D&E, MNC@Ca/MnCO₃/ARV particles did not significantly alter the LPO levels in DC2.4, whereas a significant increase in LPO levels was observed in B16 cells. This indicates that MNC@Ca/MnCO₃/ARV

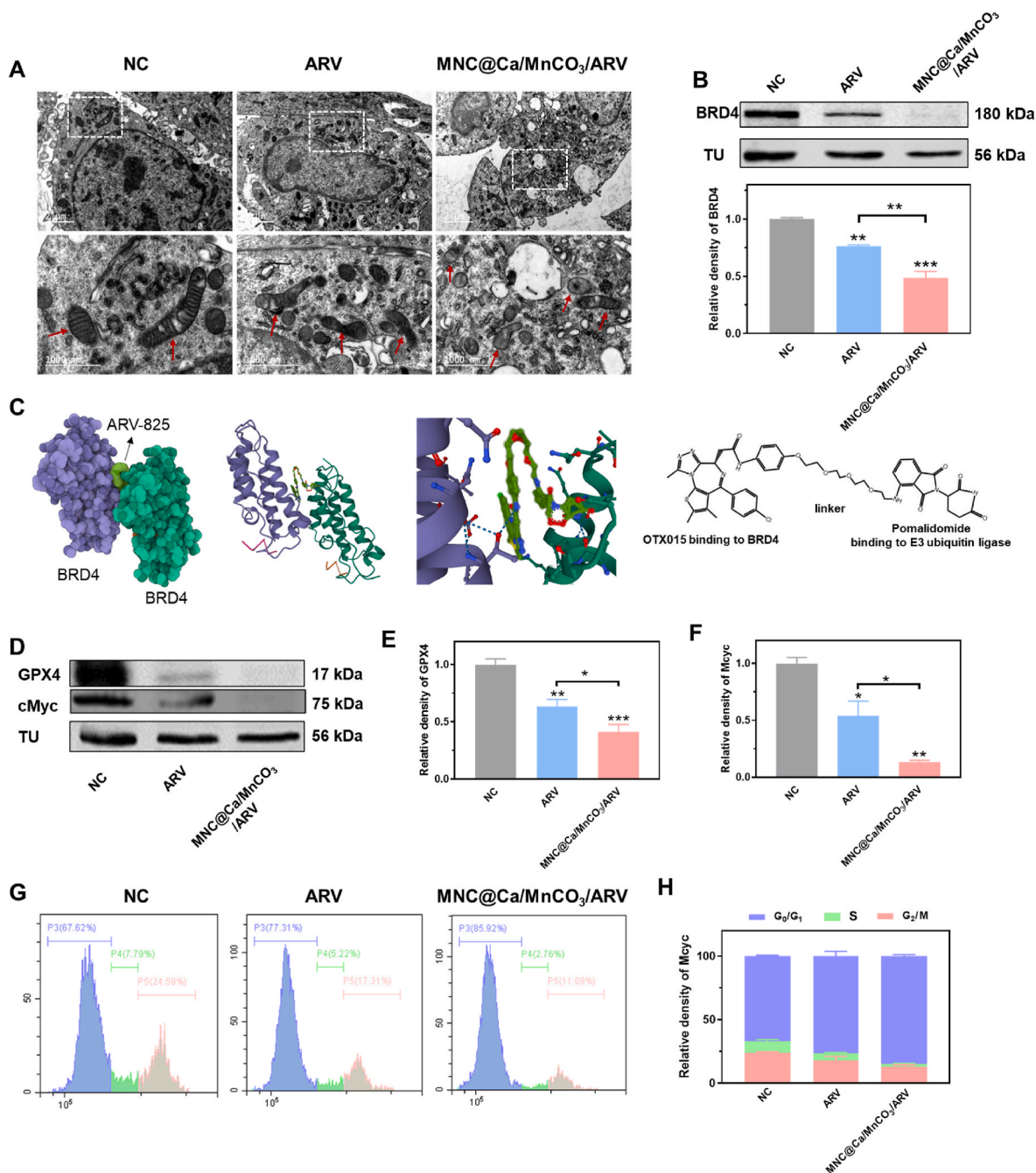


Fig. 6. (A) Mitochondrial morphology of B16 cells observed using TEM. (B) The relative BRD4 protein level of B16 cells and corresponding statistical analysis in each group. (C) The molecular docking diagram of ARV-825 and BRD4. (D–F) The GPX4 and cMyc protein levels of B16 cells and corresponding statistical analysis. (G–H) The cell cycle of B16 cells and corresponding statistical analysis. * $P < 0.05$, ** $P < 0.01$, *** $P < 0.001$.

particles did not induce ferroptosis in normal immune cells DC2.4 but significantly promoted the specific ferroptosis in B16 tumor cells. This selective effect may be attributed to the high expression of BRD4 in melanoma cells (Supporting Information Figures S4A&B). As an important oncogene, BRD4 is typically expressed at higher levels in tumor cells than in normal cells. Therefore, the drug ARV-825 can specifically degrade BRD4, which is particularly evident in B16 cells, thereby enhancing the ferroptosis-inducing effect mediated by MNC@Ca/MnCO₃/ARV particles. This result demonstrates their ability to selectively promote ferroptosis within tumor cells without affecting the functional integrity of normal immune cells.

BRD4 is a cytosolic protein associated with chromatin, that affects DNA replication and cell cycle progression [24,26]. On the one hand, the

degradation of BRD4 leads to the decline of ROS eliminator glutathione peroxidase 4 (GPX4), which results in a decrease in mitochondrial membrane potential and a dramatic increase in ROS [24]. On the other hand, the degradation of BRD4 inhibits the expression of cMyc, which affects cell proliferation and cell cycle. First, the molecular docking analysis was performed to assess the binding affinity of the ARV-825 for protein BRD4. As shown in Fig. 6C. The results show that ARV-825 binds specifically to BRD4 through OTX015 with a binding energy as low as -9.476 kcal/mol, indicating that the binding of ARV-825 to BRD4 was very stable. Then, the E3 ubiquitin ligase in the structure of ARV-825 will recruit E3 ubiquitinase, which will promote the degradation of BRD4. To examine whether ARV-825 can degrade BRD4 after entering cells, the BRD4 content of B16 cells after treatment with different

preparations was examined by Western blotting analysis. As shown in Fig. 6B, ARV-825 entering cells could bind and degrade BRD4, and the loading of ARV-825 by MNC@Ca/MnCO₃ nanoparticles further increased the degradation of BRD4. Due to that the loading of ARV-825 by nanoparticles significantly promotes the uptake of ARV-825 by cells. The degradation of cMyc and GPX4 was then analyzed with the western blot analysis, as shown in Fig. 6D–F. Compared with the control group, the cMyc and GPX4 protein content in ARV and MNC@Ca/MnCO₃/ARV groups significantly declined, and MNC@Ca/MnCO₃/ARV group declined the most. These results indicate that the degradation of BRD4 by MNC@Ca/MnCO₃/ARV nanoparticles directly affects the expression of cMyc and GPX4, which affects the normal cell cycle and causes ferroptosis. Then, the cell cycle assays were performed and the results showed that the MNC@Ca/MnCO₃/ARV nanoparticles affected DNA replication, and arrested cell cycle in G0/G1 phase (Fig. 6G and H), which will affect cell normal growth, and cause cell death.

2.6. Ferroptosis of tumor cells enhanced the maturation of BMDCs and antigen presentation

Ferroptosis can induce immunogenic cell death (ICD), releasing damage-associated molecular patterns (DAMPs), high mobility group box 1 (HMGB1), and mainly including calmodulin (CRT), which serves as an “eat me” signal, and then recruits APCs to promote anti-tumor immune responses [27,28]. This study further examined whether inducing ferroptosis in tumor cells enhances the activation of bone marrow-derived cells (BMDCs) and the presentation of tumor antigens. The isolated BMDCs were treated with the above B16 cell supernatant of each group for 24 h, after which the levels of major histocompatibility complex (MHC) and costimulatory molecules in the cells were assessed (Fig. 7A). As illustrated in Fig. 7B–G, compared to the supernatant from the control group, the supernatant from the ARV and MNC@Ca/MnCO₃/ARV groups significantly upregulated the expression levels of MHC II, MHC I, CD86, CD80, and CD40 on BMDCs. Furthermore, the expression levels of MHC II, CD86, and CD40 induced by the supernatant

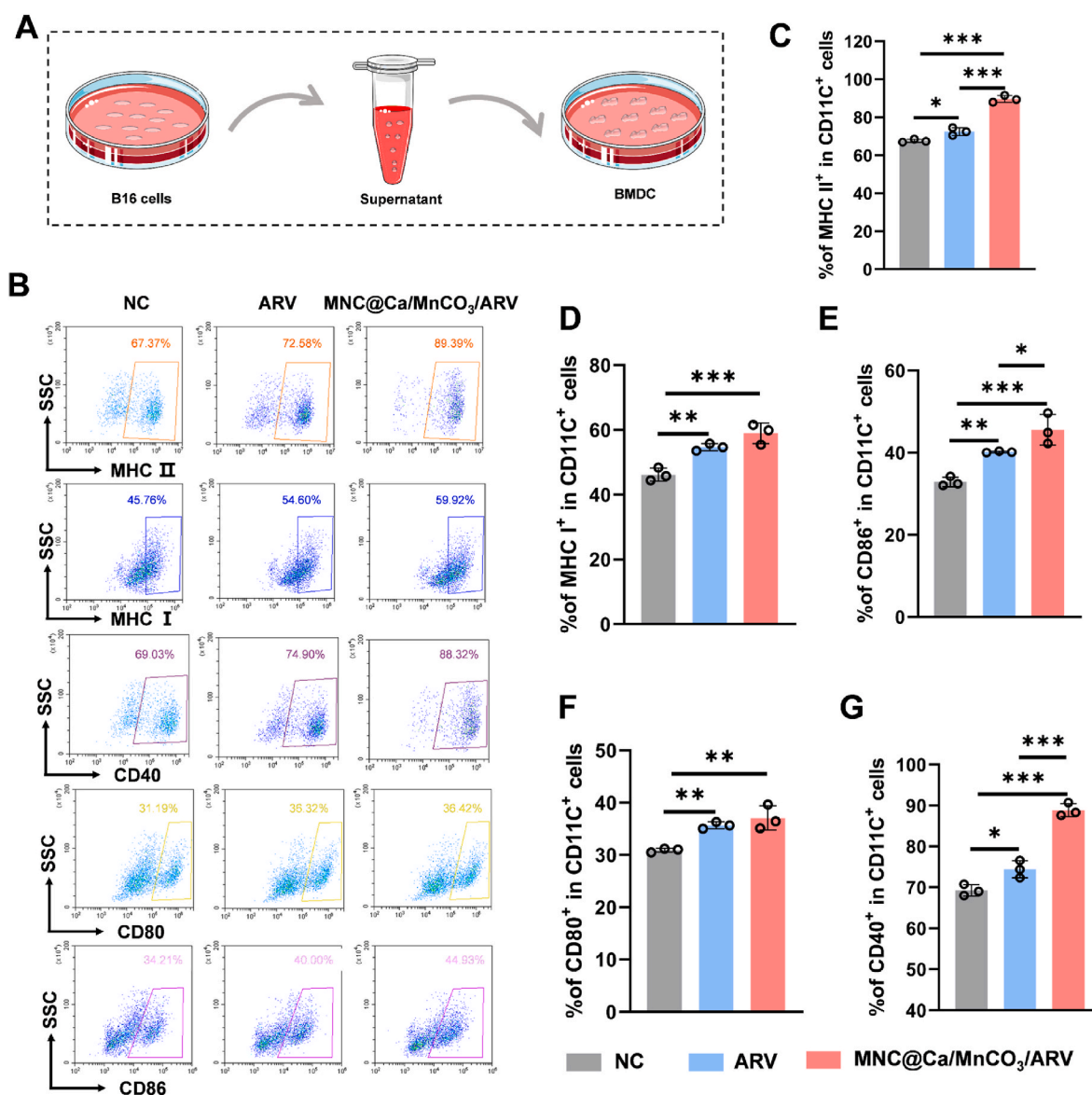


Fig. 7. DC activation and antigen presentation. (A) BMDC stimulation protocol in vitro. After stimulating BMDC in vitro with a supernatant of B16 cells, the expression of OVA-specific MHC I, MHC II, and co-stimulating molecules on BMDCs was detected by using the flow cytometer. (B) Flow scatter plot of each experimental group, and the corresponding percentages of (C–G) MHC II, MHC I, CD86, CD80, and CD40 molecules expressed on CD11c⁺ DC cells. *P < 0.05, **P < 0.01, ***P < 0.001.

from the MNC@Ca/MnCO₃/ARV group were significantly higher than those induced by the ARV group. These findings suggest that loading ARV onto MNC@Ca/MnCO₃ nanoparticles effectively induces the ICD, promotes antigen presentation, and activates BMDCs, thereby facilitating subsequent immune responses.

2.7. Magnetic nanoparticles capture the antigen to enhance antigen presentation

Antigen uptake by APCs initiates antigen presentation, triggering specific immune responses. To assess the effectiveness of MNC@Ca/MnCO₃ nanoparticles in capturing and delivering antigens, we utilized

the model antigen-ovalbumin (OVA). [Supporting Information Figures S1B&C](#) demonstrates the efficient absorption of Cy5.5-labeled OVA by MNC@Ca/MnCO₃ nanoparticles, showing red fluorescence. Furthermore, effective antigen capture by DCs is crucial for robust immune responses [29]. Thus, we evaluated the antigen delivery capability of MNC@Ca/MnCO₃ nanoparticles. As shown in CLSM images of [Fig. 8A](#), the red fluorescence of the Cy5.5-OVA alone group was extremely weak, whereas the red fluorescence of the MNC@Ca/MnCO₃/Cy5.5-OVA group was strong and overlapped with the green fluorescence of the lysosomes, suggesting that MNC@Ca/MnCO₃ nanoparticles could deliver abundant antigen into the cytosolic lysosomes of DC. Subsequently, we used MNC@Ca/MnCO₃/Cy5.5-OVA

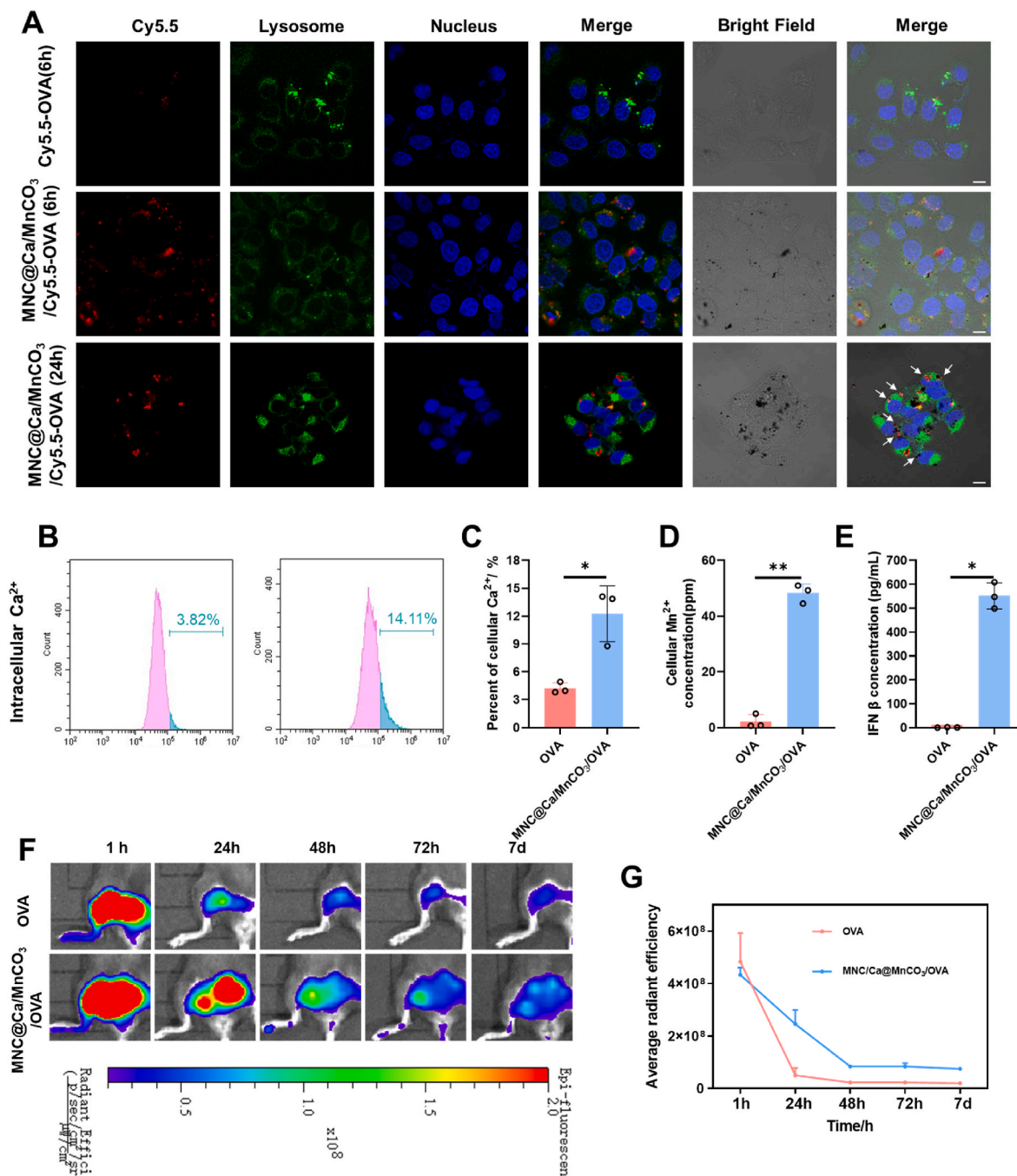


Fig. 8. (A) CLSM images of DC 2.4 after incubation with Cy5.5-OVA and MNC@Ca/MnCO₃/Cy5.5-OVA for different times. (B, C) Intracellular Ca²⁺ level of DCs after incubation with OVA and MNC@Ca/MnCO₃/OVA. (D) Intracellular Mn²⁺ levels of DCs after incubation with OVA and MNC@Ca/MnCO₃/OVA. (E) The level of cytokines IFN β secreted by DCs in each group. (F, G) Observation of antigen at the vaccination site and corresponding mean fluorescence intensity from each group of mice. Scar bar: 20 μm *P < 0.05, ***P < 0.001.

nanoparticles co-cultured with DC2.4 cells for 24 h, and examined the escape of the antigen from the lysosomes. As shown in Supporting Information Fig. 8A, the red fluorescence of the antigen was significantly separated from the green fluorescence of the lysosome (as indicated by the white arrow), indicating that the antigen successfully escaped from the lysosome. This separation was attributed to the fact that the lysosomes promoted the degradation of the MNC@Ca/MnCO₃ nanoparticles, thereby releasing the antigen, which would have contributed to the efficiency of antigen cross-presentation.

2.8. The degradation of MNC@Ca/MnCO₃ nanoparticles in the DC promotes antigen cross-presentation

Effective degradation of vaccine vectors in the cytoplasm is crucial for the controlled release of antigens and adjuvants. Therefore, intracellular Mn²⁺ and Ca²⁺ of DC were examined to detect whether the nanoparticles were degraded. The results are shown in Fig. 8B–D, nanoparticles can significantly increase the intracellular Mn²⁺ and Ca²⁺ levels, which indicates that MNC@Ca/MnCO₃ nanoparticles can be degraded in the cells. Moreover, intracellular Mn²⁺ functions as an immune adjuvant, promoting the generation of type I interferon [30],

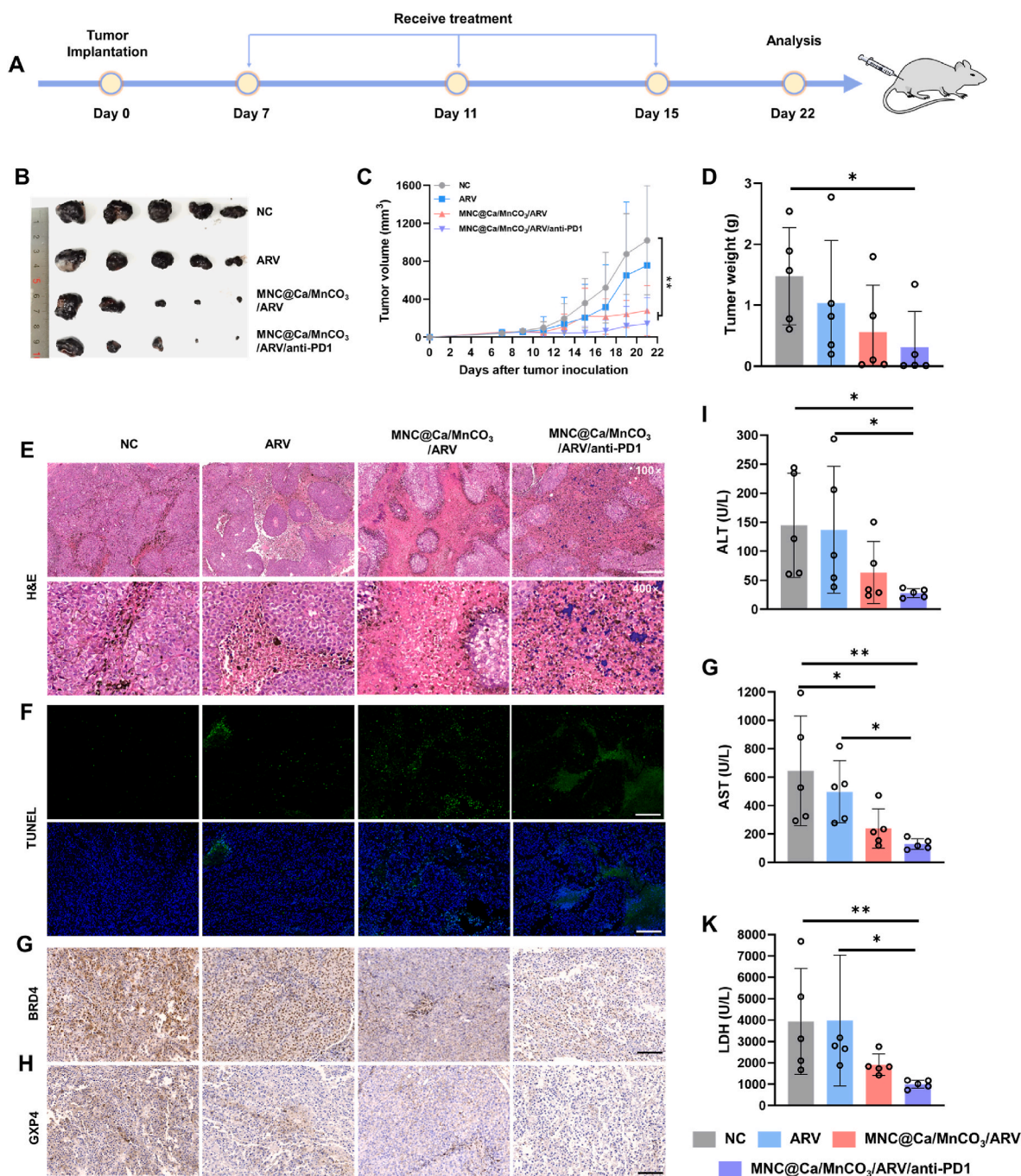


Fig. 9. In vivo inhibition of melanoma tumors by treatment with MNC@Ca/MnCO₃/OVA/anti-PD1 system. (A) The schematic diagram of anti-tumor therapy. (B) The digital photograph of the tumor, (C) average tumor growth curves, and (D) tumor weights from each group of mice. The (E) H&E and (F) TUNEL staining images of tumors from each group of mice. (G) BRD4 and (H) GXP4 immunohistochemical staining images of tumors from each group of mice. (I–K) The level of ALT, AST, and LDH in serum. Scale bars = 100 μm *P < 0.05, **P < 0.01.

thereby enhancing CD8⁺ T cell-induced immune responses [31]. Among them, Interferon- β (IFN- β) is a typical type I-IFN that can effectively detect whether the STING pathway is activated. Here, IFN- β secretion levels in DC supernatants of each group were detected. As shown in Fig. 8E, the IFN- β concentration was notably elevated in the MNC@Ca/MnCO₃/OVA group compared to the OVA alone group. These results suggest that MNC@Ca/MnCO₃ nanoparticles, which act as carriers and adjuvants, can be slowly degraded in cells to facilitate the release of the adjuvant Mn²⁺ and promote antigen cross-presentation.

2.9. Magnetic nanoparticles extend antigen retention time at the injection site

Prolonged residence time of antigens at the administration site is essential for sustained immune stimulation. To assess tumor antigen (OVA) retention, mice were subcutaneously injected with Cy5.5-OVA and MNC@Ca/MnCO₃/Cy5.5-OVA formulations, and their fluorescence intensity was monitored over time. As illustrated in Fig. 8F–G, the fluorescence intensity of Cy5.5-OVA alone decreased rapidly within 24 h post-immunization and was barely visible on day 7. In contrast, the MNC@Ca/MnCO₃/Cy5.5-OVA group exhibited robust fluorescence at 24 h, with a slower decline by day 7, indicating prolonged antigen retention facilitated by MNC@Ca/MnCO₃ nanoparticles. Furthermore, efficient co-delivery of antigen and adjuvant to the same antigen-presenting cells (APCs) enhances their synergy.

2.10. In situ tumor vaccines enhance anti-tumor efficacy In vivo

Since MNC@Ca/MnCO₃/ARV had outstanding inhibitory effects on B16 cells, its efficacy was further explored in tumor-bearing mice (Fig. 9A). Throughout tumor therapy, alterations in tumor volume and changes in the body weights of mice were consistently monitored every 2 days. Tumor growth status as shown in Fig. 9B and C, ARV-825 alone had a better tumor inhibitory effect in the early stage (before day 13), but in the late stage of tumor growth, the inhibitory effect on tumor growth was minimal, which may be attributed to the very poor water solubility of ARV-825, resulting in its low bioavailability in the tumor. On the contrary, the MNC@Ca/MnCO₃/ARV-containing group showed significant tumor inhibitory effects at all stages of tumor growth, which may be because ARV-825 loaded by MNC@Ca/MnCO₃ nanoparticles improves the bioavailability of ARV-825 and prolongs its retention time in the tumor. In addition, the tumor growth was slower in MNC@Ca/MnCO₃/ARV/anti-PD1 group than MNC@Ca/MnCO₃/ARV group. The corresponding tumor-bearing mice of each group were shown in Supporting Information Figure S3A. Moreover, the tumor weight was significantly lighter in the MNC@Ca/MnCO₃/ARV/anti-PD1 group than the saline group (Fig. 9D), and all mice showed no significant fluctuations in body weight (Supporting Information Figure S3B). These suggested that the loading of ARV and anti-PD1 on MNC@Ca/MnCO₃ nanoparticles enhances the tumor treatment effect.

In addition, we added a mixed-treatment group (ARV-825 + anti-PD1) as an additional control group and conducted another animal study. As shown in Supporting Information Figure S12A, ARV-825 alone did not significantly inhibit tumor growth, possibly due to its poor water solubility. While the mixed-treatment group demonstrated some anti-tumor effects, primarily because the PD1 antibody enhanced immune cell function for more effective tumor cell attack and killing, this effect was still inferior to that of the final system. There was no significant difference in the body weight of mice in all groups (Supporting Information Figure S12B). The final system exhibited the best anti-tumor performance due to the integrated functions of all components, working synergistically to strengthen the anti-tumor immune response. The carrier not only improved the water solubility and stability of ARV-825 but also loaded tumor antigens to construct an in situ tumor vaccine, acting as an adjuvant. Coupled with the PD1 antibody, it promoted anti-tumor immunotherapy, achieving complementary advantages between

chemotherapy and immunotherapy.

Several blood biochemical indicators, namely AST, ALT, and LDH, serve as markers to gauge the efficacy of melanoma treatment across different groups [32–35]. As shown in Fig. 9I–K, the level of AST in the MNC@Ca/MnCO₃/ARV group was notably reduced compared to those in the saline group. In addition, in comparison to both the saline and ARV groups, the levels of AST, ALT, and LDH in the MNC@Ca/MnCO₃/ARV/anti-PD1 group were significantly decreased. These results indicated that the loading of ARV and PD1 by MNC@Ca/MnCO₃ nanoparticles could improve anti-tumor ability. For H&E staining, tumor tissue in the control group had more viable cells, while the MNC@Ca/MnCO₃/ARV and MNC@Ca/MnCO₃/ARV/anti-PD1 group showed obvious tumor cell death (Fig. 9E). Meanwhile, the TUNEL staining showed that MNC@Ca/MnCO₃/ARV and MNC@Ca/MnCO₃/ARV/anti-PD1 induced more tumor cell apoptosis (Fig. 9F). These results further suggest that MNC@Ca/MnCO₃ nanoparticles loaded with ARV-825 and anti-PD1 can effectively improve the anti-tumor effect.

To further investigate the activity of ARV-825 in inducing ferroptosis in vivo, the changes of BRD4 and GPX4 in tumors were then examined. As shown in Fig. 9G and H, ARV-825 containing group treatment downregulated the BRD4 and GPX4 protein expression in tumors. Moreover, ARV-825 loaded by MNC@Ca/MnCO₃ nanoparticles further reduced the expression of BRD4 and GPX4 protein, which is consistent with the results in vitro. These observations suggest that MNC@Ca/MnCO₃/ARV can effectively induce ferroptosis and suppress tumor growth.

2.11. In situ tumor vaccines enhance anti-tumor immune response In vivo

Based on the fact that MNC@Ca/MnCO₃/ARV/anti-PD1 produced significant treatment of tumors, we speculate that it may have successfully constructed a vaccine in the in situ tumor and triggered a strong systemic anti-tumor cellular immune response. To test whether the system could induce ICD in tumors, we examined CRT in tumor tissues, which is a “eat me” signal for tumor cells [27]. As shown in Fig. 10A, the red fluorescence of CRT in saline and ARV alone groups was very low, whereas the red fluorescence of CRT in MNC@Ca/MnCO₃/ARV containing groups was significantly increased, which indicates that ARV-825 loaded by MNC@Ca/MnCO₃ nanoparticles can contribute to the induction of tumor immunogenic death. Successful induction of ICD of tumor will ultimately promote infiltration of effective T cells in the tumor, which is essential for cancer immunotherapy. Thus, CD8⁺ T cell infiltration in the tumor was examined. As shown in Fig. 10B, there was an elevation in the percentage of CD8⁺ T cells within the tumors of the ARV-containing group compared to the saline group. Notably, the highest percentage of CD8⁺ T cells was observed in the tumors of the MNC@Ca/MnCO₃/ARV/anti-PD1 group. This may be because MNC@Ca/MnCO₃/ARV nanoparticles increased ICD levels, Mn²⁺ acted as an immune adjuvant, and anti-PD1 inhibited the immune escape of tumor cells.

Antigen-specific antibody titers are a key indicator for evaluating the intensity and type of immune response. Specifically, an increase in IgG1 titers indicates an enhanced cell-mediated immune responses, whereas an increase in IgG2a titers indicates an enhanced humoral immune response [36]. As depicted in Fig. 10G–I, compared with the saline alone group, the IgG and IgG2a titer of MNC@Ca/MnCO₃/ARV and MNC@Ca/MnCO₃/ARV/anti-PD1 groups significantly increased. Moreover, the IgG1 titers were highest in the MNC@Ca/MnCO₃/ARV/anti-PD1 group. These findings suggest that MNC@Ca/MnCO₃ nanoparticles loaded with ARV-825 and anti-PD1 can activate both cellular and humoral immune responses and produce specific antibodies after killing the tumor cells, successfully constructing an in situ tumor vaccine.

The transport of tumor antigens taken up by APCs to immune tissues such as lymph nodes and spleens is an important step in activating T cells and promoting antibody production. Therefore, the levels of antigen

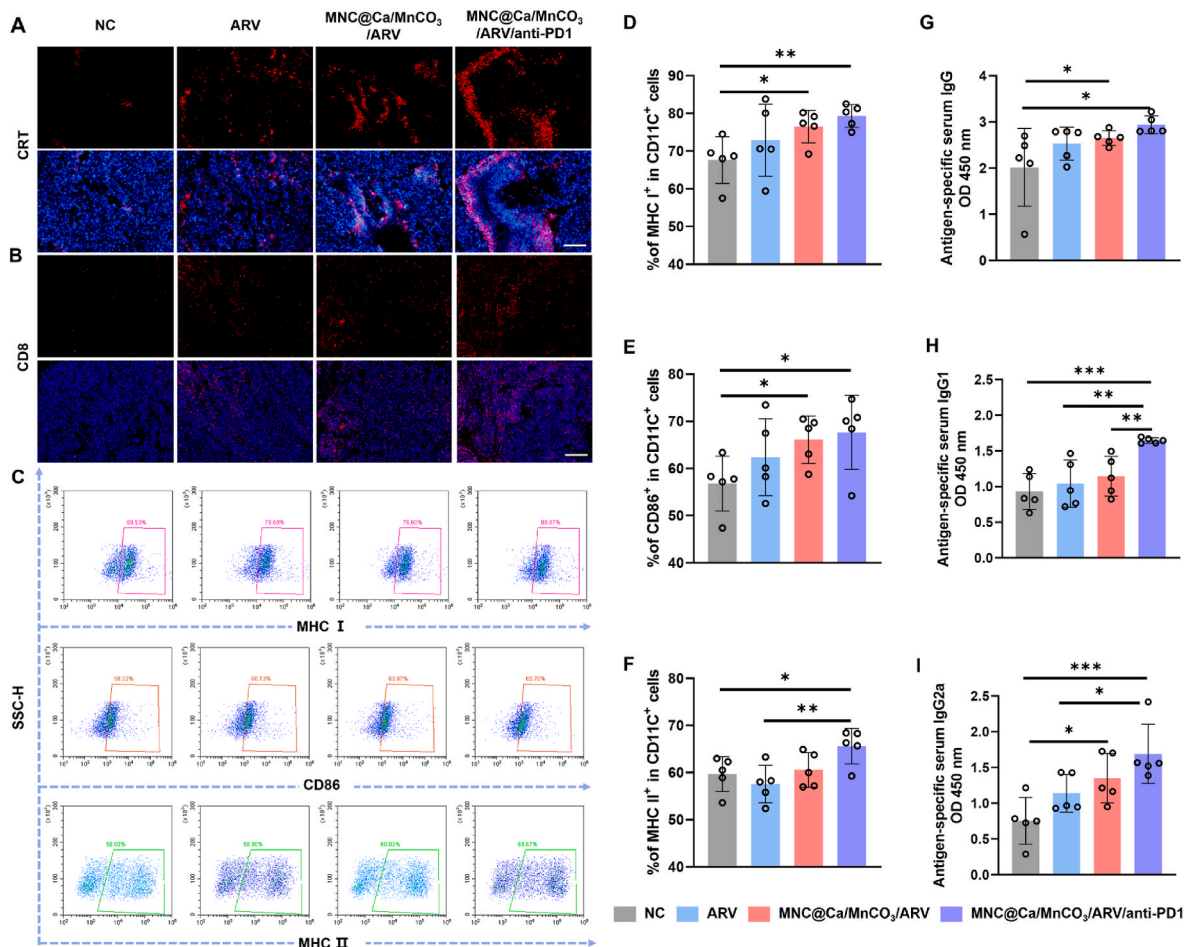


Fig. 10. (A) The CRT and (B) CD8⁺ T cell staining images of tumors from each group of mice. (C–F) Flow scatter plots of MHC I, MHC II, and co-stimulating molecules on BMDCs from splenocytes, and the corresponding statistical results. (G–I) The titer levels of antigen-specific IgG, IgG1, and IgG2a. Scale bars = 100 μ m *P < 0.05, **P < 0.01, ***P < 0.001.

OVA reaching the spleen were detected using immunohistochemical analysis. As depicted in Supporting Information Figures S4A&B, the OVA amounts in the spleens of saline and ARV alone groups were low, while the OVA amounts in the MNC@Ca/MnCO₃-containing groups were high. Notably, the OVA amounts of the MNC@Ca/MnCO₃/ARV/anti-PD1 group were the highest. That is to say, MNC@Ca/MnCO₃ nanoparticles loaded with ARV and anti-PD1, after killing tumor cells, promoted the arrival of the tumor antigens to the spleen, which would promote tumor antigen presentation. Subsequently, the activation and antigen presentation of DCs in the spleens were examined. As illustrated in Fig. 10C–F, the ARV-alone group did not exhibit a significant enhancement in the expression of CD86 and MHC I in DCs compared to the saline group. In contrast, the group treated with MNC@Ca/MnCO₃ nanoparticles demonstrated a significant increase in the expression of CD86 and MHC I in DCs, consistent with the *in vitro* findings (Fig. 7B–G). This may be attributed to the fact that loading of ARV-825 by MNC@Ca/MnCO₃ nanoparticles would increase the tumor-killing effect and the adjuvant effect of Mn²⁺ in the nanoparticles further activated DCs and antigen cross-presentation. Furthermore, there was a notable increase in MHC II molecules observed in the MNC@Ca/MnCO₃/ARV/anti-PD1 group compared to the saline group. This finding further indicates that anti-PD1 treatment may enhance antigen delivery even more effectively.

The spleens contain a large number of immune cells that are crucial in inducing immune responses [37]. Upon encountering the same antigen again, these cells undergo rapid proliferation, enabling T cells to mount a swift and potent immune response [38]. To test whether

splenocytes from immunized mice have an immune memory function, the splenocytes were first co-incubated with B16 cells (Fig. 11A). As shown in Fig. 11B, compared with saline and ARV alone groups, the numbers of splenocytes adhering to tumor cells were higher in MNC@Ca/MnCO₃ containing groups. The results of the quantitative assessment of the toxicity of splenocytes to tumor cells are shown in Fig. S11, the splenocytes in the ARV-825 group alone were essentially non-toxic to tumor cells compared to the control group, whereas the splenocytes in the MNC@Ca/MnCO₃/ARV and MNC@Ca/MnCO₃/ARV/anti-PD1 groups caused significant toxicity to tumor cells, with the splenocytes in the MNC@Ca/MnCO₃/ARV/anti-PD1 group's splenocytes were the most toxic to tumor cells. These findings suggest that MNC@Ca/MnCO₃/ARV and MNC@Ca/MnCO₃/ARV/anti-PD1 treatments were able to more effectively stimulate the body to generate tumor-specific immune responses, where the addition of anti-PD1 further enhanced this effect. This may be attributed to the fact that cytotoxic T-lymphocytes in the splenocytes of MNC@Ca/MnCO₃ containing groups were proliferated and differentiated in large numbers and the blockage of immune escape by anti-PD1. Subsequently, the percentages of CD8⁺ T cells in splenocytes were assessed, as depicted in Fig. 11C and D. Compared to the saline group, the inclusion of ARV significantly elevated the proportion of CD8⁺ T cells in splenocytes. Notably, the MNC@Ca/MnCO₃/ARV/anti-PD1 group exhibited the highest percentage of CD8⁺ T cells in splenocytes. Moreover, the sizes of lymph nodes in the ARV-loaded nanoparticle groups were enlarged (Supporting Information Figure S5C), which indicates that T-lymphocytes in the lymph nodes proliferated and differentiated in large

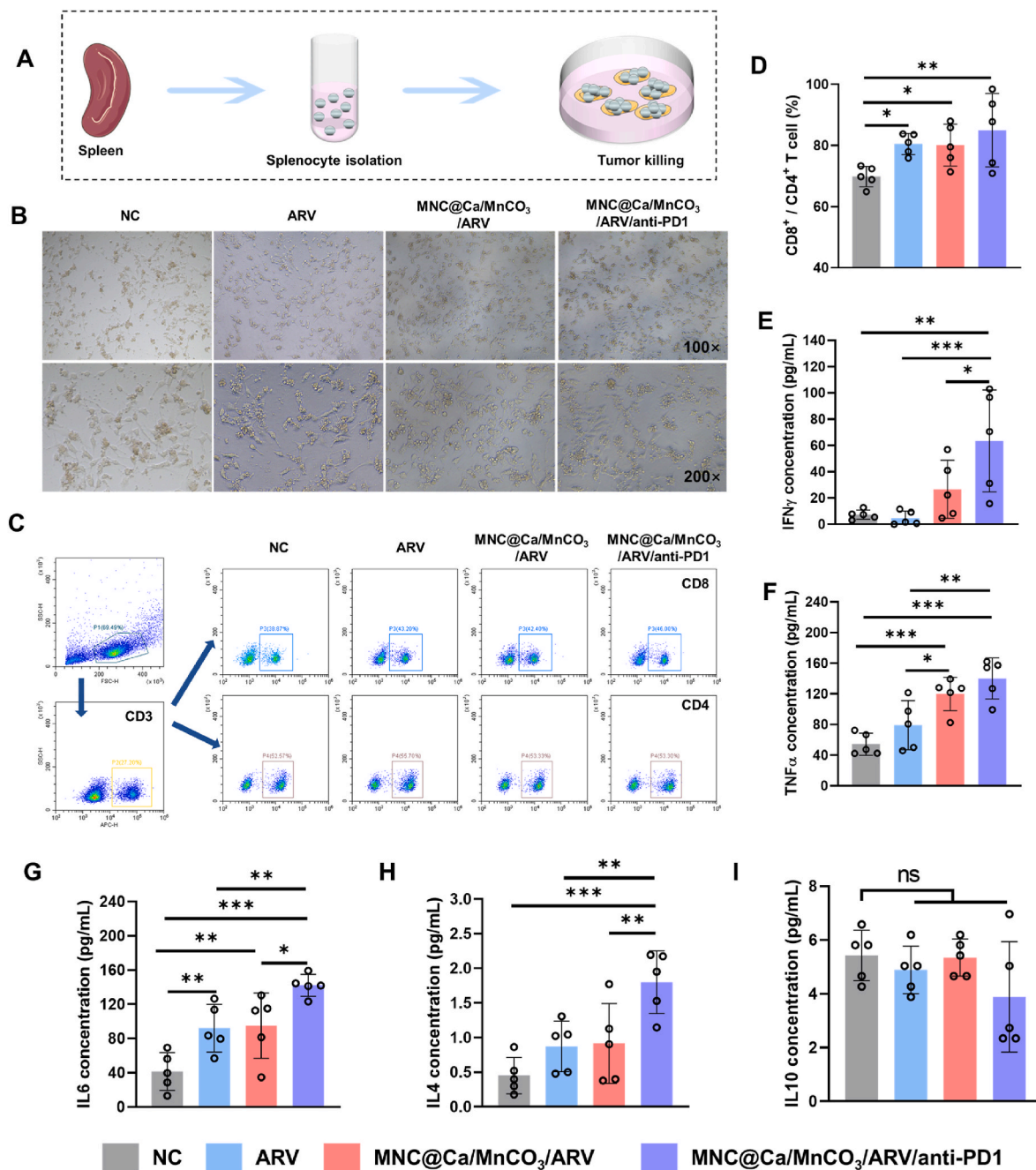


Fig. 11. (A) Schematic diagram of co-cubation of splenocytes with B16 cells. (B) The cell morphology of splenocytes co-cubated with B16 cells. (C, D) The rates of CD8⁺/CD4⁺ T cells in splenocytes. (E–I) The level of cytokines IFN-γ, TNF-α, IL-6, IL-4, and IL-10 in the splenocytes supernatant detected by ELISA. *P < 0.05, **P < 0.01, ***P < 0.001.

numbers. Subsequently, the antigens were used to stimulate the splenocytes again, and the secretion of cytokines by these splenocytes was assessed, as depicted in Fig. 11E–I. In comparison to the saline group, the levels of Tumor necrosis-α factor (TNF-α) and Interleukin-6 (IL-6) were notably elevated in the ARV-containing groups. Moreover, compared with the saline and ARV alone group, the levels of IFNγ, TNF-α, IL-6 and IL-4 in the MNC@Ca/MnCO₃/ARV/anti-PD1 group were significantly higher. Furthermore, the secretion levels of IL-10 were comparable across all groups, suggesting that MNC@Ca/MnCO₃/ARV and anti-PD1 treatments did not induce immunomodulatory effects to suppress the expression of these antitumor-associated cytokines. These findings indicate that the encapsulation of ARV-825 and anti-PD1 within MNC@Ca/MnCO₃ nanoparticles promotes the secretion of cytokines

associated with cellular and humoral immunity, and also indicate that MNC@Ca/MnCO₃ nanoparticles loaded with ARV-825 and anti-PD1 can enhance the immune memory function of mice, which can make an immediate immune response when stimulated by antigen again.

The elevated proportion of memory T cells stands out as a crucial hallmark of vaccination, as these cells assume a pivotal role in immune surveillance, which can respond quickly and efficiently to re-exposed antigens [39]. Memory T cells consist of two distinct subgroups, namely central memory T cells (T_{CM} cells, CD44^{high} CD62L^{high}) and effector memory T cells (T_{EM} cells, CD44^{high} CD62L^{low}) [40]. The results of T_{EM} cell proportions are shown in Supporting Information Figures S5A&B, MNC@Ca/MnCO₃/ARV/anti-PD1 group could increase the percentages of CD4⁺ and CD8⁺ T_{EM} cells, which suggested that

MNC@Ca/MnCO₃ nanoparticles loaded with ARV-825 and anti-PD1 induced the production of immune memory T cells. Together, these results suggested that tumors treated with MNC@Ca/MnCO₃/ARV/anti-PD1 can successfully construct an in situ tumor vaccine, which enhances antigen presentation, promotes the proliferation and differentiation of T-lymphocytes, and enhances the level of immune response.

Finally, the biosafety of the above formulations was tested in vivo. The hearts, livers, spleens, lungs, and kidneys of these mice were

harvested for histopathological analysis, and the corresponding H&E staining outcomes were illustrated in Supporting Information Figure S6. All organs showed no obvious pathological changes, indicating that MNC@Ca/MnCO₃/ARV/anti-PD1 nanoparticles have good biosafety.

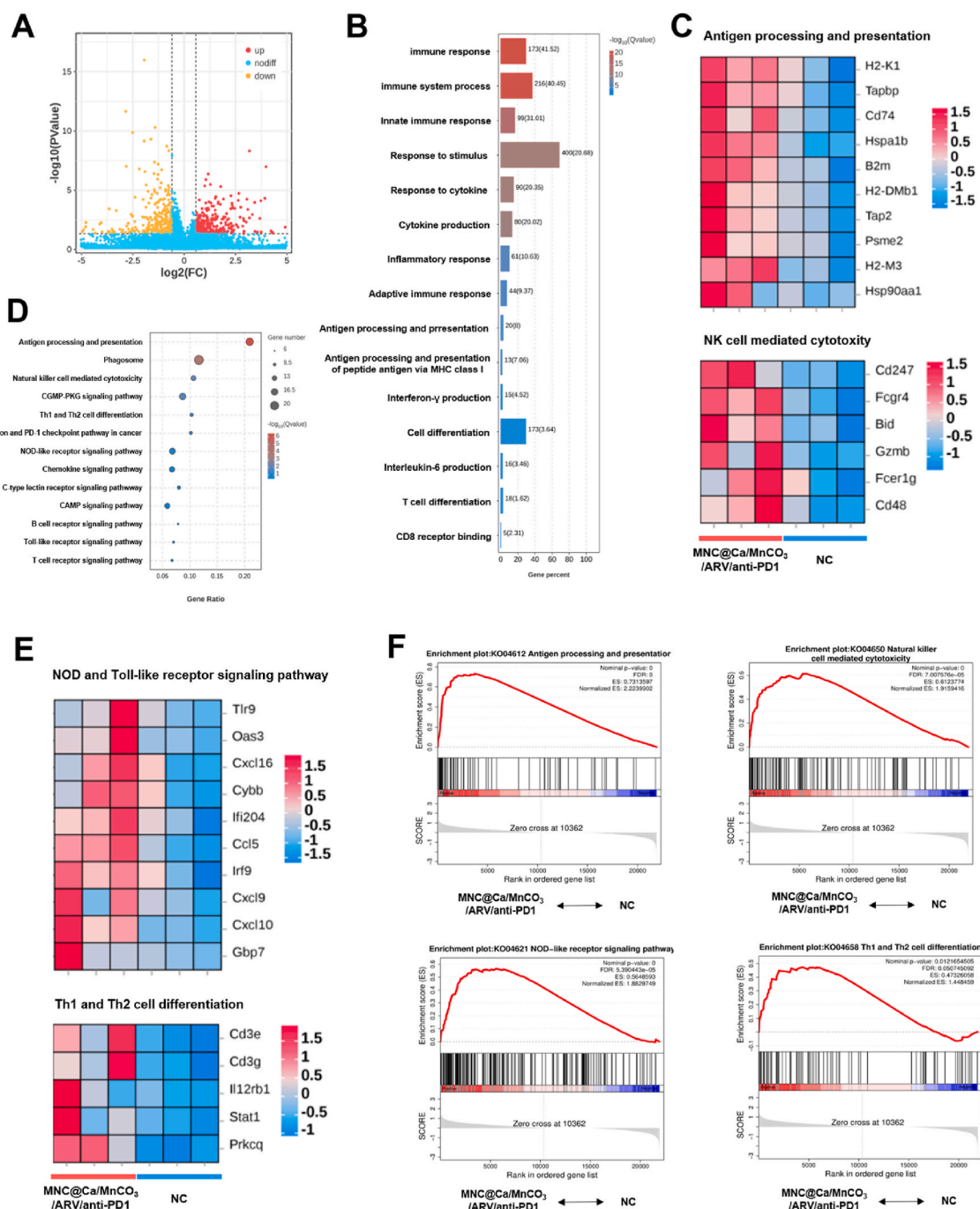


Fig. 12. RNA-seq analysis of tumors after treatment with MNC@Ca/MnCO₃/ARV/anti-PD1. (A) Volcano map of differentially expressed genes between the control and MNC@Ca/MnCO₃/ARV/anti-PD1 groups (n = 3). The x-axis was the log₂ scale of the fold change of gene expression. The y-axis was the minus log₁₀ scale of p values, indicating the significant expression difference level. (B) Gene Ontology (GO) analysis of up- and downregulated genes. Gene ratio (shown in orange) and $-\log_{10}(\text{Pvalue})$ of all GO terms were shown. (C, E) GO network analysis of significantly upregulated genes in tumors from the MNC@Ca/MnCO₃/ARV/anti-PD1-treated mice, as compared with the control mice. The color from blue to red indicated that the gene expression was from low to high. (D) KEGG enrichment analysis. (F) Representative pathways enriched in the identified genes as determined by GSEA. (For interpretation of the references to color in this figure legend, the reader is referred to the Web version of this article.)

2.12. *In situ* tumor vaccines remodel the tumor immune microenvironment

Sustained tumor regression typically necessitates a synergistic blend of innate and adaptive immune responses. NK cells and macrophages are indispensable components of innate immunity, while CD4⁺ T cells and CD8⁺ T cells are pivotal for orchestrating the adaptive immune response [41]. To further elucidate the potential mechanism for enhancing anti-tumor immune responses by MNC@Ca/MnCO₃/ARV/PD1-constructed *in situ* tumor vaccines, the RNA-sequencing (RNA-seq)-based transcriptome analysis of treated tumors was conducted. As shown in Fig. 12 A, a total of 615 differentially expressed genes were identified, with 311 genes showing significant up-regulation and 304 genes showing down-regulation. Subsequent Gene Ontology (GO) and Kyoto Encyclopedia of Genes and Genomes (KEGG) functional enrichment analyses revealed significant enrichment of pathways associated with the activation of innate and adaptive immune responses. These pathways include antigen processing and presentation, T cell differentiation, natural killer cell-mediated cytotoxicity, differentiation of Th1 and Th2 cells, NOD-like receptor signaling pathway, Toll-like receptor signaling pathway, as well as T and B cell receptor signaling pathway (Fig. 12B and D&F). As shown in the gene heatmap, many immune response-related genes promoting anti-tumor were significantly up-regulated, including H2-K1, H2-M3, Hsp90aa1, CD247, FCGR1A, CXCL9, CXCL10, IRF9, CD3e, and CD3g (Fig. 12C and E).

To more effectively control tumors and inhibit their metastasis and recurrence, the body needs to establish a robust and sustained anti-tumor immune response. This process relies on the synergistic action of multiple genes and signaling pathways to ensure effective recognition and destruction of tumor cells as well as continuous immune surveillance. First, up-regulated MHC-I molecules (e.g., H2-K1 and H2-M3) together with TAPBP (Tapasin) facilitate antigen presentation to CD8⁺ T cells, a critical step in the recognition and destruction of tumor cells. Increased expression of these molecules ensures that tumor-specific antigens are efficiently presented to CTLs, thereby initiating a direct killing mechanism against tumor cells. Secondly, upregulation of the chemokines CCL5, CXCL9, and CXCL10 plays a role in recruiting more effector T cells to the tumor site [42]. These chemokines direct T cells and other immune cells towards tumor infiltration, maintaining a constant immune surveillance environment and ensuring that emerging tumor cells do not escape the surveillance of the immune system. In addition, the upregulation of Hsp90 protein accelerates the speed of immune cells to reach the lesion site and improves the clearance efficiency of immune cells against tumor cells [43]. These will enhance the local anti-tumor immune response. The presence of memory T cells is critical for the long-term prevention of tumor recurrence, as they can be rapidly activated upon tumor reappearance to provide a rapid and effective immune response. In particular, upregulation of CD247 and FCGR1 protein expression helps APCs recognize antigens in tumors and initiate immune surveillance against tumors [44]. This enhanced antigen recognition is important for the initiation of adaptive immune responses and the generation of specific immune memory. IRF9 and STAT1, as part of the interferon signaling pathway, further enhance anti-tumor immunity by promoting both innate and adaptive immune responses. Finally, CD3e and CD3g are present on the surface of T-lymphocytes as part of the TCR-CD3 complex, and are essential for activating T-cells and initiating adaptive immune responses [45]. Their presence ensures the sensitivity of T cells to antigenic stimuli, which is particularly critical for controlling tumor metastasis. Together, these genes work through different mechanisms to enhance the body's immune surveillance of tumors, reverse the immunosuppressive tumor microenvironment, and reduce the risk of tumor metastasis and recurrence.

2.13. *In situ* tumor vaccines prevent the tumor lung metastases

We established a mouse metastasis model by tail vein injection of melanoma cells (Supporting Information Figure S13A). On day 18 after injection, all experimental animals showed lung metastasis. The results were shown in Supporting Information Figures S13B&C, ARV-825 alone failed to significantly reduce the number of black metastatic foci on the lungs or lymph nodes, indicating that it was largely ineffective in inhibiting tumor metastasis, which may be related to its failure to effectively activate the body's immune system. In contrast, the group treated with MNC@Ca/MnCO₃/ARV complex showed significant anti-metastatic effects, with a significant reduction of metastatic foci on the lungs and lymph nodes. In particular, the most significant improvement was observed in the group treated with MNC@Ca/MnCO₃/ARV/anti-PD1 nanoparticles: a 74.8 % reduction in lung metastases compared to the control group. This result suggests that the MNC@Ca/MnCO₃/ARV/anti-PD1 nanoparticles effectively inhibited melanoma metastasis by enhancing the systemic anti-tumor immune response.

3. Conclusions

In this study, a magnetic tumor antigen capture system MNC@Ca/MnCO₃/ARV/anti-PD1 was constructed, using PROTAC drug to avoid injuring APCs, specifically degrading BRD4 and GPX4 of tumor cells, significantly induce ferroptosis and release a large amount of tumor antigens. Meanwhile, magnetic nanoparticles have a strong adsorption effect on tumor antigens to achieve *in situ* capture of tumor antigens and form pathogen-like micro-nanoparticles to promote the retention of tumor antigens. Moreover, Mn²⁺ in the particles acted as an adjuvant to promote antigen cross-presentation, and together with the PD1 antibody, enhanced the anti-tumor effect of the *in situ* tumor vaccine, successfully reversing the immunosuppressive tumor microenvironment. In this study, the tumor-specific ferroptosis based on PROTAC drug-induced and magnetically driven antigen capture strategy provided a new strategy for enhancing the tumor *in situ* vaccine effect.

4. Methods

4.1. Materials

Manganese chloride monohydrate (MnCl₂·H₂O), sodium carbonate (Na₂CO₃), and Calcium chloride (CaCl₂) were sourced from Macklin (Shanghai, China). ARV-825 was obtained from MedChemExpress (USA). 1640 RPMI culture medium and fetal bovine serum were obtained from Gibco (CA, USA). Crystalline violet stain, CCK-8, dichlorodihydro-fluorescein diacetate (DCFH-DA), dihydroethidium (DHE), JC-1, annexin V-FITC/PI double dye kits, Calcein-AM/PI double dye kits, lysotracker Red, BCA protein detection kit, red blood cell lysis buffer, and DAPI staining solution were obtained from Beyotime (Shanghai, China). Anti-BRD4 rabbit antibody, anti-cMyc rabbit antibody, anti-GPX4 rabbit antibody, FITC-Tunnel cell apoptosis detection kit, CD8-GB13429, and anti-calreticulin (CRT) rabbit antibody were obtained from Servicebio (Wuhan, China). Murine IL-4 and granulocyte-macrophage colony-stimulating factor (GM-CSF) were obtained from PeproTech (NJ, USA). All enzyme-linked immunosorbent assay (ELISA) kits and flow cytometry antibody dyes were purchased from BioLegend (CA, USA). All female C57BL/6 mice (4–6 weeks) were purchased from Beijing HPK Laboratory Animal Technology Co. (Beijing, China). Liperfluo was purchased from Dojindo (Kyushu, Japan). LumiKine Xpress mIFN-β 2.0 enzyme-linked immunosorbent assay (ELISA) kit was obtained from InvivoGen (CA, USA).

4.2. Synthesis of MNC nanoparticles

Firstly, potassium citrate (0.4 g) and FeCl₃ (0.65 g) were dissolved in

ethylene glycol (40 mL) and stirred vigorously for 1 h at room temperature. Subsequently, sodium acetate (1.2 g) was added and stirred for 30 min. Then, the mixture was added to the Teflon-lined autoclave for 12 h at 200 °C. Finally, the products were collected, washed with ethanol and water three times, and freeze-dried for storage.

4.3. Synthesis and characterization of MNC@Ca/MnCO₃ nanoparticles

Initially, 5 mg of MNC nanoparticles were combined with a mixture of MnCl₂ and CaCl₂ (0.016 M) in glycerol/water solutions (v/v = 1/1, 10 mL) and stirred for 30 min. Subsequently, the glycerol/water solution containing NH₄HCO₃ (0.16 M, 10 mL) was introduced to the mixture and stirred for 1 h at 50 °C, followed by washing the precipitate three times. Finally, the precipitate underwent characterization using a transmission electron microscope (TEM, JEM-2010HR, Japan), scanning electron microscope (SEM, Zeiss, Germany), laser nanoparticle sizer (Malvern, Britain), inductively coupled plasma optical emission spectrometer (ICP, Thermo iCAP 7000, US), X-ray powder diffractometer (XRD, Miniflex 600, Japan), vibrating sample magnetometer (Lake-Shore, USA), Fourier transform infrared spectrometer (FT-IR, VER-TEX70, Germany), a specific surface area and porosity analyzer (ASAP 2460, Micromeritics, USA) and X-ray photoelectron spectroscopy (XPS, Thermo Scientific Escalab 250Xi).

4.4. The loading and release of ARV-825

Firstly, a dispersion of 5 mg of MNC@Ca/MnCO₃ nanoparticles was prepared in 1 mL of deionized water. Then, the ARV-825 (1 mg, dissolved in 10 µL DMSO) was added into the suspensions and stirred for 72 h. After centrifugation, the supernatant was utilized to detect the free ARV-825 concentration using a microplate reader (BIOTEK, USA).

The MNC@Ca/MnCO₃/ARV (50 µg) nanoparticles were suspended in 100 µL of PBS with different pH values (7.4 and 5.5) and shaken (50 rpm) at 37 °C. At designated time intervals, samples were centrifuged to remove the supernatant and resuspended with 100 µL of fresh PBS, followed by the detection of the fluorescence intensity (FI) of the suspension using the microplate reader to calculate the release ratio of ARV-825.

The MNC@Ca/MnCO₃/ARV nanoparticles (1 mg) were dispersed in deionized water (1 mL). Then, the anti-PD1 solution (10 µL, 100 µg) was added to the suspensions and stirred for 72 h. After centrifugation, the free anti-PD1 in the supernatant was detected with BCA kits.

4.5. Cell viability detection

B16 and DC2.4 cells were seeded into 96-well plates at a density of 1×10^4 cells/well, and incubated for 24 h. Following incubation, the cells were treated with various concentrations of ARV or MNC@Ca/MnCO₃/ARV formulations (ARV: 0, 50, 100, 200, 500, 1000, and 2000 ng/mL) for an additional 24 h. Additionally, DC2.4 cells were exposed to different concentrations of MNC@Ca/MnCO₃ formulations (0, 0.1, 0.25, 0.5, 0.75, and 1 mg/mL) or MNC@Ca/MnCO₃/ARV formulations (ARV: 0, 50, 100, 200, 500, 1000, and 2000 ng/mL) for 24 h. Cell viability was subsequently assessed by the addition of CCK-8 dye.

B16 cells were seeded into 24-well plates at a density of 5×10^4 cells/well and incubated for 24 h. Following incubation, the cells were treated with either ARV or MNC@Ca/MnCO₃/ARV formulations (ARV: 200 ng/mL) for an additional 24 h. Subsequently, the cell morphology was examined using an optical microscope (Leica DMI6000, Germany), and the cells were harvested and stained with annexin V-FITC/PI dyes. The stained cells were then analyzed using a flow cytometer (Beckman Coulter, USA). Additionally, B16 cells treated with ARV or MNC@Ca/MnCO₃/ARV formulations were stained with Calcein-AM/PI dyes, and the viability of the cells was assessed by observing live and dead cells using a fluorescence microscope (DMRA2, Leica, Germany).

4.6. Migration experiment

B16 cells were seeded in 12-well plates (1×10^5 cells/well), and incubated at 37 °C. Once the cells reached 100 % confluence, a scratch with a width of approximately 400 µm was drawn in a certain direction with a sterile 200 µL pipet tip. Then, the cells were exposed to ARV or MNC@Ca/MnCO₃/ARV formulations for 24 h. Finally, the changes in the scratches were observed under the optical microscope at regular intervals.

4.7. Cell uptake and cellular co-localization

B16 cells were cultured in cell culture dishes at a density of approximately 5×10^4 cells/dish and allowed to incubate for 24 h. Following this, the cells were treated with ARV or MNC@Ca/MnCO₃/ARV formulations and incubated for 6 h. Subsequently, the cells were stained with Lyso-Tracker red fluorescent dye for 2 h, fixed for 20 min, and then further stained with DAPI dye for 5 min. The cells were visualized using a confocal laser scanning microscope (CLSM, Zeiss, Germany).

For another set of experiments, B16 cells were seeded in 24-well plates at a density of 5×10^4 cells/well and incubated for 24 h. Following this, the cells were treated with ARV or MNC@Ca/MnCO₃/ARV formulations and incubated for 6 h. The cells were then collected and analyzed using a flow cytometer (Beckman Coulter, USA).

4.8. Cell cycle progression assay

B16 cells were plated in 24-well plates and subjected to the same treatment as described above. After 24 h, the cells were harvested and fixed in 70 % ethanol for 12 h. Subsequently, the cells were washed and stained with propidium iodide (PI) for 15 min. The cell cycle distribution was then analyzed using the flow cytometer.

4.9. Western blotting assay

B16 cells were cultured in 10-cm dishes at a density of 2×10^6 cells/dish and subjected to the same treatment as described above. Following treatment, the cells were lysed using a lysis buffer, and the protein content of the lysed cells was normalized using the BCA kit. Subsequently, the protein samples were separated by SDS-PAGE and transferred onto polyvinylidene difluoride (PVDF) membranes. The PVDF membranes were then incubated in a blocking buffer containing 5 % (w/v) bovine serum albumin (BSA). Following blocking, the membranes were probed with anti-BRD4, anti-GPx4, and anti-cMyc antibodies (dilution ratio = 1:1000) overnight, followed by incubation with secondary antibodies (dilution ratio = 1:10,000) for 2 h. The signal intensities of BRD4, GPx4, and cMyc were subsequently measured using a dual-color infrared laser imaging system (Odyssey CLX, USA).

4.10. Intracellular ROS, O₂⁻ and LPO detection assay

B16 cells were seeded in 24-well plates and subjected to the same treatment as described previously. Following the designated treatment duration, the cells were washed and subsequently stained with DCFH-DA, DHE and Liperfluo dye solution. Subsequently, the stained cells were visualized under the fluorescence microscope, and the fluorescence intensities were quantitatively analyzed using Image J software.

In addition, DC2.4 and B16 cells were seeded in 24-well plates and treated with MNC@Ca/MnCO₃/ARV nanoparticles for 24 h. Then, the cells were washed and stained with Liperfluo dye solution. Finally, the stained cells were visualized under the fluorescence microscope, and the fluorescence intensities were quantitatively analyzed using Image J software.

4.11. Measurement of mitochondrial membrane potential ($\Delta\psi_m$)

The B16 cells underwent the previously outlined procedure. After the designated treatment period, the cells were stained with JC-1 dye and analyzed using both a flow cytometer and a fluorescence microscope.

4.12. Mitochondria morphology observation

B16 cells were seeded in 10-cm dishes and treated with ARV or MNC@Ca/MnCO₃/ARV formulations. After 24 h, the cells were harvested and suspended in 2 mL of glutaraldehyde solution. Subsequently, the cells were embedded in resin, sectioned, and examined under the TEM to observe changes in mitochondrial morphology.

4.13. DC maturation *in vitro*

B16 cells were processed as described above. Subsequently, the cell supernatant of B16 was gathered and co-cultured with BMDCs for 24 h. Subsequently, the BMDCs were harvested and incubated with FITC-anti-CD11c, APC-anti-CD80, PE-anti-MHC II, PerCP-Cy5.5-*anti*-CD80, or PE-anti-MHC I solutions for 30 min. Finally, the BMDCs were analyzed using the flow cytometer.

4.14. Antigen capture *in vitro*

Initially, MNC@Ca/MnCO₃ nanoparticles (5 mg) were introduced into the OVA antigen solution (in physiological saline, 1 mg/mL, 1 mL) and agitated at 25 °C. Subsequently, the free OVA was assessed using the BCA kit at various time intervals. Following this, DC2.4 cells were cultured with MNC@Ca/MnCO₃/OVA for 6 h or 24 h, washed three washes, and then exposed to Lyso-Green fluorescent dye solution for 2 h. Subsequently, the cells were fixed with a 4% paraformaldehyde solution for 20 min and then stained with a DAPI staining solution for 5 min. The prepared samples were examined using the CLSM.

4.15. The intracellular levels of Mn²⁺ and Ca²⁺

The DC2.4 cells were seeded in 6-well plates at a density of 5×10^5 cells/well and incubated for 24 h. The cells were then incubated for an additional 24 h with OVA or MNC@Ca/MnCO₃/OVA formulations. Afterward, the cells were exposed to cell lysis buffer, and the supernatant was then harvested and diluted to 5 mL. The Mn content in the supernatant was measured using an inductively coupled plasma-atomic emission spectrometer (iCAP 7000, Thermo, USA). To detect intracellular Ca²⁺ levels, the cells were harvested and stained with Flo-4 AM staining solution for 30 min. Finally, the cells were analyzed using the flow cytometer.

4.16. Detection of IFN- β

The BMDCs were seeded in 24-well plates at a density of 5×10^4 cells/well and incubated for 24 h with OVA or MNC@Ca/MnCO₃/OVA formulations. The supernatants were harvested and analyzed for IFN- β levels using an ELISA kit.

4.17. Retention time of captured antigen at the injection site

C57BL/6 female mice were immunized with Cy5.5-OVA or MNC@Ca/MnCO₃/Cy5.5-OVA preparations, respectively. The antigen fluorescence intensity at the injection site was observed with a small animal bioluminescence imaging system (IVIS Lumina III, PerkinElmer, USA).

4.18. Therapeutic efficacy of the *in situ* tumor vaccine

All experiments involving animals were conducted to the ethical

policies and procedures approved by the ethics committee of the Animal Care Committee of the Jinan University (Approval No. SYXK 2022-0174). Tumor vaccine was evaluated in female C57BL/6 mice (4–6 weeks old) divided into four groups (n = 5). On day 0, B16 cells were subcutaneously injected into the back of the mice. Then, 100 μ L of saline, ARV, MNC@Ca/MnCO₃/ARV, or MNC@Ca/MnCO₃/ARV/anti-PD1 formulations were injected into the tumor at day 7, 11, and 15, and the tumor volumes and body weights of the mice were measured with one-day intervals, tumor volume = (width² × length)/2. The tumors, sera, and spleens of the mice were collected on day 22. An automatic biochemical analyzer (Chemray 240, Rryto, China) was used to measure the levels of lactate dehydrogenase (LDH), alanine aminotransferase (ALT) and aspartate aminotransferase (AST) in the sera. The titers of tumor antigen-specific antibodies in the sera were measured using ELISA. The tumor slices were stained with CRT, hematoxylin-eosin (H&E), CD8-GB13429, and TUNEL dye solutions, and observed with the fluorescence microscope.

The spleens and tumor slices were then further analyzed by immunohistochemistry. The distribution of antigen OVA in the spleens and the distribution of the BRD4 or GPX4 in tumors were observed by an optical microscope (Leica DMI6000, Germany). The tissue slices of the main organs, including the heart, liver, spleen, lung, and kidney, were stained with an H&E staining solution, and observed with the optical microscope.

Splenocytes were obtained and seeded in 96-well plates at a concentration of 1×10^5 cells/well, and co-incubated with B16 cells at a concentration of 1×10^4 cells/well for 24 h. Subsequently, these cells were washed, and their morphology was observed with a microscope. In addition, the obtained splenocytes were seeded in 12-well plates at a concentration of 5×10^5 cells/well and re-stimulated for 60 h with OVA antigen solution. After that, the cell supernatants were collected and analyzed using ELISA kits to measure the secretion levels of cytokines IFN- γ , TNF- α , IL-10, IL-6, and IL-4 in the supernatants. In addition, the splenocytes separated from the spleens were stained for 30 min with fluorescent dye-labeled antibodies (APC-anti-CD62L, PE-anti-CD44, PerCP-Cy5.5-*anti*-CD80 and FITC-anti-CD4, FITC-anti-CD11c, PE-anti-MHC II, or PE-anti-MHC I) and detected with the flow cytometer.

4.19. Mouse tumor RNA sequencing and gene expression analysis

The above tumors were rapidly collected and frozen with liquid nitrogen. The mRNA samples of the control and MNC@Ca/MnCO₃/ARV/anti-PD1 groups were used for RNA sequencing (GENEDENOVO, Guangzhou, China). The Omicsmart online platform was used to perform functionally related GO terms analysis, Kyoto Encyclopedia of Genes and Genomes (KEGG) enrichment analysis, gene set enrichment analysis (GSEA), and quantification of differential gene expression analysis.

4.20. *In vivo* anti-metastasis capability

The female C57BL/6 mice (4–6 weeks old, n = 5 for each group) were divided into four groups (n = 5). On day 0, B16-OVA cells were subcutaneously injected into the back of the mice. Then, 100 μ L of saline, ARV, MNC@Ca/MnCO₃/ARV, or MNC@Ca/MnCO₃/ARV/anti-PD1 formulations were injected into the tumor at day 7, 11, and 15. In addition, C57BL/6 mice were injected intravenously with B16-OVA melanoma cells (1×10^6 per mouse) at day 7. The lungs and lymph nodes of the mice were collected on day 25 for observation of tumor metastasis.

4.21. Statistical analysis

The experimental data were expressed as mean \pm standard deviation (SD). Significance levels were indicated as follows: Statistical analysis was performed using GraphPad Prism 5 software, and the differences

between the groups were analyzed using a one-way ANOVA test. * $P < 0.05$, ** $P < 0.01$, and *** $P < 0.001$.

CRediT authorship contribution statement

Linghong Huang: Writing – original draft, Investigation, Formal analysis, Data curation. **Xinyuan Sun:** Investigation, Formal analysis, Data curation. **Qinhua Zuo:** Investigation, Formal analysis. **Ting Song:** Validation, Investigation. **Ning Liu:** Validation, Resources, Investigation. **Zonghua Liu:** Writing – review & editing, Resources, Methodology, Funding acquisition, Formal analysis. **Wei Xue:** Writing – review & editing, Supervision, Project administration, Funding acquisition.

Availability of data and materials

The datasets generated during and/or analyzed during the current study are available from the corresponding author on reasonable request.

Funding

This work was financially supported by the National Natural Science Foundation of China (82404556 and 32471525), Science and Technology Program of Guangzhou (202103030004), and Basic and Applied Basic Research Foundation of Guangdong Province (2022A1515012148 & 2023A1515011221).

Declaration of competing interest

The authors declare no conflict of interest.

Acknowledgments

Authors thank the Centric Laboratory of Medical College of Jinan University and the Department of Biomedical Engineering of Jinan University for providing experimental and instrument platforms.

Appendix A. Supplementary data

Supplementary data to this article can be found online at <https://doi.org/10.1016/j.mtbio.2025.101523>.

Data availability

Data will be made available on request.

References

- M.F. Segura, B. Fontanals-Cirera, A. Gaziol-Sovran, M.V. Guijarro, D. Hanniford, G. Zhang, P. González-Gomez, M. Morante, L. Jubierre, W. Zhang, F. Darvishian, M. Ohlmeyer, I. Osman, M.M. Zhou, E. Hernandez, BRD4 sustains melanoma proliferation and represents a new target for epigenetic therapy, *Cancer Res.* 73 (20) (2013) 6264–6276.
- X. Wei, Y. Li, P. Luo, Y. Dai, T. Jiang, M. Xu, Y. Hao, C. Zhang, Y. Liu, Development and validation of robust ferroptosis-related genes in myocardial ischemia-reperfusion injury, *Journal of cardiovascular development and disease* 10 (8) (2017) 344.
- S. Sui, J. Zhang, S. Xu, Q. Wang, P. Wang, D. Pang, Ferritinophagy is required for the induction of ferroptosis by the bromodomain protein BRD4 inhibitor (+)-JQ1 in cancer cells, *Cell Death Dis.* 10 (5) (2019) 331.
- J.J. Luke, K.T. Flaherty, A. Ribas, G.V. Long, Targeted agents and immunotherapies: optimizing outcomes in melanoma, *Nat. Rev. Clin. Oncol.* 14 (8) (2017) 463–482.
- L. Galluzzi, A. Buqué, O. Kepp, L. Zitvogel, G. Kroemer, Immunogenic cell death in cancer and infectious disease, *Nat. Rev. Immunol.* 17 (2) (2017) 97–111.
- T.L.V. Aaes, A. Kaczmarek, T. Delvaeye, B. De Craene, S. De Koker, L. Heyndrickx, I. Delrue, J. Taminiau, B. Wiernicki, P. De Groot, Vaccination with necroptotic cancer cells induces efficient anti-tumor immunity, *Cell Rep.* 15 (2) (2016) 274–287.
- J. Wu, D.J. Waxman, Immunogenic chemotherapy: dose and schedule dependence and combination with immunotherapy, *Cancer Lett.* 419 (2018) 210–221.
- Y. Li, K. Zhang, Y. Wu, Y. Yue, K. Cheng, Q. Feng, X. Ma, J. Liang, N. Ma, G. Liu, G. Nie, L. Ren, X. Zhao, Antigen capture and immune modulation by bacterial outer membrane vesicles as in situ vaccine for cancer immunotherapy post-photothermal therapy, *Small* 18 (14) (2022) e2107461.
- Y. Zhang, S. Ma, X. Liu, Y. Xu, J. Zhao, X. Si, H. Li, Z. Huang, Z. Wang, Z. Tang, W. Song, X. Chen, Supramolecular assembled programmable nanomedicine as in situ cancer vaccine for cancer immunotherapy, *Adv. Mater.* 33 (7) (2021) e2007293.
- Injectable adhesive hydrogel as photothermal-derived antigen reservoir for enhanced anti-tumor immune, *Adv. Funct. Mater.* (2021) 1–16.
- B. Dale, M. Cheng, K.S. Park, J. Jin, Advancing targeted protein degradation for cancer therapy, *Nat. Rev. Cancer* (2021) 638–654.
- M. Békés, D.R. Langley, C.M. Crews, PROTAC targeted protein degraders: the past is prologue, *Nat. Rev. Drug Discov.* 21 (3) (2022) 181–200.
- Y. Fang, G. Liao, B. Yu, Small-molecule MDM2/X inhibitors and PROTAC degraders for cancer therapy: advances and perspectives, *Acta Pharm. Sin. B* 10 (7) (2020) 1253–1278.
- B. Dale, M. Cheng, K.S. Park, H. Kaniskan, Y. Xiong, J. Jin, Advancing targeted degradation for cancer therapy, *Nat. Rev. Cancer* 21 (10) (2021) 638–654.
- S. Imaide, K.M. Riching, N. Makukhin, V. Vetma, C. Whitworth, S.J. Hughes, N. Trainor, S.D. Mahan, N. Murphy, A.D. Cowan, K.H. Chan, C. Craigan, A. Testa, C. Maniaci, M. Urh, D.L. Daniels, A. Ciulli, Trivalent PROTACs enhance protein degradation via combined avidity and cooperativity, *Nat. Chem. Biol.* 17 (11) (2021) 1157–1167.
- J. Gao, B. Hou, Q. Zhu, L. Yang, X. Jiang, Z. Zou, X. Li, T. Xu, M. Zheng, Y.H. Chen, Z. Xu, H. Xu, H. Yu, Engineered bioorthogonal POLY-PROTAC nanoparticles for tumour-specific protein degradation and precise cancer therapy, *Nat. Commun.* 13 (1) (2022) 4318.
- C. Zhang, S. He, Z. Zeng, P. Cheng, K. Pu, Smart nano-PROTACs reprogram tumor microenvironment for activatable photo-metabolic cancer immunotherapy, *Angew. Chem.* 61 (8) (2022) e202114957.
- Y. Wang, Y. Zhou, S. Cao, Y. Sun, Z. Dong, C. Li, H. Wang, Y. Yao, H. Yu, X. Song, M. Li, J. Wang, M. Wei, G. Yang, C. Yang, In vitro and in vivo degradation of programmed cell death ligand 1 (PD-L1) by a proteolysis targeting chimera (PROTAC), *Bioorg. Chem.* 111 (2021) 104833.
- L. Huang, Z. Liu, C. Wu, J. Lin, N. Liu, Magnetic nanoparticles enhance the cellular immune response of dendritic cell tumor vaccines by realizing the cytoplasmic delivery of tumor antigens, *Bioengineering & translational medicine* 8 (2) (2023) e10400.
- N. Esmaeili, P. Mohammadi, M. Abbaszadeh, H. Sheibani, Au nanoparticles decorated on magnetic nanocomposite (GO-Fe₃O₄/Dop/Au) as a recoverable catalyst for degradation of methylene blue and methyl orange in water, *Int. J. Hydrogen Energy* 44 (41) (2019) 23002–23009.
- M.A. Ghasemzadeh, M.H. Abdollahi-Basir, Fe₃O₄@ SiO₂-NH₂ nanocomposite as a robust and effective catalyst for the one-pot synthesis of polysubstituted dihydropyridines, *Acta Chim. Slov.* 63 (3) (2016) 627–637.
- A. Stoica-Guzun, M. Stroescu, S.I. Jinga, I.M. Jipa, T. Dobre, Microwave assisted synthesis of bacterial cellulose-calcium carbonate composites, *Ind. Crop. Prod.* 50 (2013) 414–422.
- Y. An, J. Zhu, F. Liu, J. Deng, X. Meng, G. Liu, H. Wu, A. Fan, Z. Wang, Y. Zhao, Boosting the ferroptotic antitumor efficacy via site-specific amplification of tailored lipid peroxidation, *ACS Appl. Mater. Interfaces* 11 (33) (2019) 29655–29666.
- L. Geng, T. Lu, H. Jing, Y. Zhou, X. Liang, J. Li, N. Li, Iron-based and BRD(4)-downregulated strategy for amplified ferroptosis based on pH-sensitive/NIR-II-boosted nano-matchbox, *Acta Pharm. Sin. B* 13 (2) (2023) 863–878.
- J.N. Moloney, T.G. Cotter, ROS signalling in the biology of cancer, *Semin. Cell Dev. Biol.* 80 (2018) 50–64.
- A. Jelinek, L. Heyder, M. Daude, M. Plessner, S. Krippner, R. Grosse, W. E. Diederich, C. Culmsee, Mitochondrial rescue prevents glutathione peroxidase-dependent ferroptosis, *Free Radic. Biol. Med.* 117 (2018) 45–57.
- X. Niu, L. Chen, Y. Li, Z. Hu, F. He, Ferroptosis, necroptosis, and pyroptosis in the tumor microenvironment: perspectives for immunotherapy of SCLC, *Semin. Cancer Biol.* 86 (3) (2022) 273–285.
- M. Zhu, M. Yang, J. Zhang, Y. Yin, X. Fan, Y. Zhang, S. Qin, H. Zhang, F. Yu, Immunogenic cell death induction by ionizing radiation, *Front. Immunol.* 12 (2021) 705361.
- L.E. Paulis, S. Mandal, M. Kreutz, C.G. Figdor, Dendritic cell-based nanovaccines for cancer immunotherapy, *Curr. Opin. Immunol.* 25 (3) (2013) 389–395.
- C. Wang, Y. Guan, M. Lv, R. Zhang, Z. Guo, X. Wei, X. Du, J. Yang, T. Li, Y. Wan, Manganese increases the sensitivity of the cGAS-STING pathway for double-stranded DNA and is required for the host defense against DNA viruses, *Immunity* 48 (4) (2018) 675–687.
- L. Zitvogel, L. Galluzzi, O. Kepp, M.J. Smyth, G. Kroemer, Type I interferons in anticancer immunity, *Nat. Rev. Immunol.* 15 (7) (2015) 405–414.
- K.-I. Lin, C.-C. Lin, S.-M. Kuo, J.-C. Lai, Y.-Q. Wang, H.-L. You, M.-L. Hsu, C.-H. Chen, L.-Y. Shiu, Carnosic acid impedes cell growth and enhances anticancer effects of carmustine and lomustine in melanoma, *Biosci. Rep.* 38 (4) (2018) BSR20180005.
- Z. Liu, J. He, T. Zhu, C. Hu, R. Bo, A. Wusiman, Y. Hu, D. Wang, Lentinan-functionalized graphene oxide is an effective antigen delivery system that modulates innate immunity and improves adaptive immunity, *ACS Appl. Mater. Interfaces* 12 (35) (2020) 39014–39023.
- R.G. Feichtinger, R. Lang, Targeting L-lactate metabolism to overcome resistance to immune therapy of melanoma and other tumor entities, *JAMA Oncol.* 2019 (2019) 2084195.

- [35] N.B. Wagner, A. Forschner, U. Leiter, C. Garbe, T.K. Eigentler, S100B and LDH as early prognostic markers for response and overall survival in melanoma patients treated with anti-PD-1 or combined anti-PD-1 plus anti-CTLA-4 antibodies, *Br. J. Cancer* 119 (3) (2018) 339–346.
- [36] T.L. Stevens, A. Bossie, V.M. Sanders, R. Fernandez-Botran, R.L. Coffman, T. R. Mosmann, E.S. Vitetta, Regulation of antibody isotype secretion by subsets of antigen-specific helper T cells, *Nature* 334 (6179) (1988) 255–258.
- [37] J.C. Jennette, H. Xiao, R.J. Falk, Pathogenesis of vascular inflammation by anti-neutrophil cytoplasmic antibodies, *J. Am. Soc. Nephrol.* 17 (5) (2006) 1235–1242.
- [38] Y. Zhang, F. Wang, E. Ju, Z. Liu, Z. Chen, J. Ren, X. Qu, Metal-organic-framework-based vaccine platforms for enhanced systemic immune and memory response, *Adv. Funct. Mater.* 26 (35) (2016) 6454–6461.
- [39] R. Ahmed, D. Gray, Immunological memory and protective immunity: understanding their relation, *Science* 272 (5258) (1996) 54–60.
- [40] R. Sahu, S. Dixit, R. Verma, S.A. Duncan, M.T. Coats, G.H. Giambartolomei, S. R. Singh, V.A. Dennis, A nanovaccine formulation of Chlamydia recombinant MOMP encapsulated in PLGA 85: 15 nanoparticles augments CD4+ effector (CD44high CD62Llow) and memory (CD44high CD62Lhigh) T-cells in immunized mice, *Nanomed. Nanotechnol. Biol. Med.* 29 (2020) 102257.
- [41] M.H. Spitzer, Y. Carmi, N.E. Reticker-Flynn, S.S. Kwek, D. Madhireddy, M. M. Martins, P.F. Gherardini, T.R. Prestwood, J. Chabon, S.C. Bendall, L. Fong, G. P. Nolan, E.G. Engleman, Systemic immunity is required for effective cancer immunotherapy, *Cell* 168 (3) (2017) 487–502.
- [42] R. Reschke, T.F. Gajewski, CXCL9 and CXCL10 bring the heat to tumors, *Science immunology* 7 (73) (2022) 6509.
- [43] C. Lin, Y. Zhang, K. Zhang, Y. Zheng, L. Lu, H. Chang, H. Yang, Y. Yang, Y. Wan, S. Wang, M. Yuan, Z. Yan, R. Zhang, Y. He, G. Ge, D. Wu, J. Chen, Fever promotes T lymphocyte trafficking via a thermal sensory pathway involving heat shock protein 90 and $\alpha 4$ integrins, *Immunity* 50 (1) (2019) 137–151.
- [44] X. Huang, T. Tang, G. Zhang, T. Liang, Identification of tumor antigens and immune subtypes of cholangiocarcinoma for mRNA vaccine development, *Mol. Cancer* 20 (1) (2021) 50.
- [45] A. Singh, S. Dees, I.S. Grewal, Overcoming the challenges associated with CD3+ T-cell redirection in cancer, *Br. J. Cancer* 124 (6) (2021) 1037–1048.